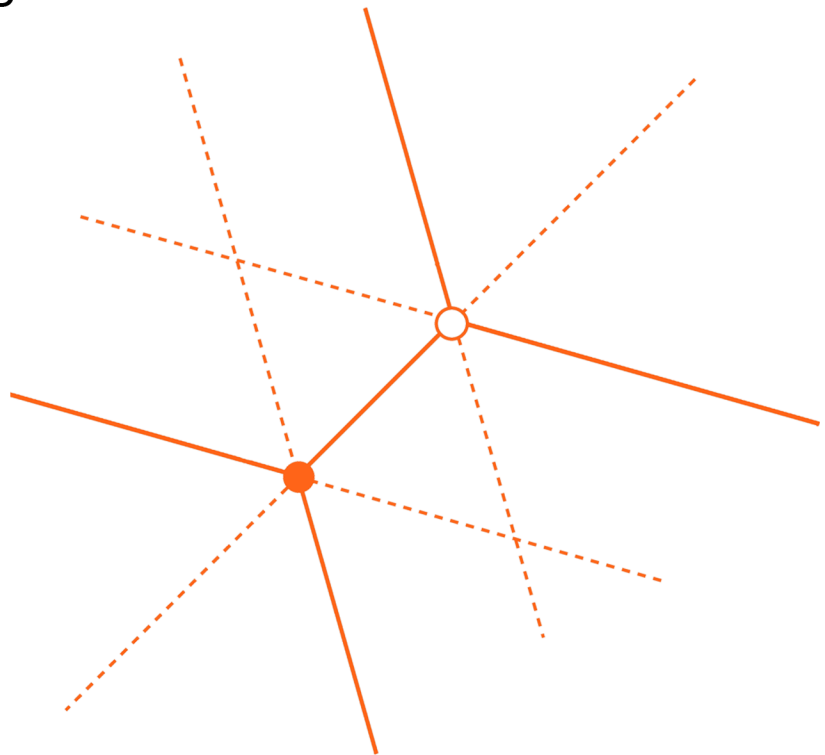


Single Charge Transport and Charge Sensing in Quantum Dots

Bachelor of Science Thesis
Electrical Engineering

Fotios Avgidis
March 2016



Graduation committee

Dr. ir. F.A. Zwanenburg
Dr. S.V. Amitonov
Dr. ir. C. Salm

ABSTRACT

As we approach the theoretical limit of the transistor size, finding new ways to process digital information is crucial. A computing device that exploits the laws of quantum mechanics can potentially achieve significant speed-up over its classical counterparts in certain problems and applications. Based on the proposal of using the spin orientation of a single electron trapped in a semiconductor quantum dot as a carrier of classical information, we investigate the charge transport in single and double quantum dots defined by the electrostatic gating of a carrier gas in silicon for cryogenic temperatures. Furthermore, we demonstrate that the gated quantum dot can act as a single-charge transistor and as a charge sensor. We report experiments and findings on two devices with different architecture, for both electron and hole transport down to the few-charge regime.

CONTENTS

1. Introduction	6
1.1 Quantum Computation	6
1.2 Spin as a Qubit	6
1.3 Quantum Dots	8
1.4 Charge Sensing	9
1.5 Outline of the Thesis	9
2. Theory	10
2.1 Tunneling Through a Potential Barrier	10
2.2 Heisenberg Uncertainty Principle	12
2.3 Coulomb Blockade	13
2.4 Tunnel Junctions	14
2.5 Requirements for Coulomb Blockade	14
2.6 Single Quantum Dot Circuit Model.....	15
2.7 Charge Transport in Quantum Dots	18
2.8 Stability Diagrams in the Low-Bias Regime	21
2.9 Stability Diagrams in the High-Bias Regime	23
2.10 Charge Transport in Double Quantum Dots	24
3. Fabrication & Experimental Methods	33
3.1 Device Architecture	33
3.2 Device Fabrication	35
3.3 Measurement Setups	39
4. Results & Discussion	41
4.1 Electron Transport on Device I.....	41
4.2 Electron Transport on Device II	48
4.3 Hole Transport on Device II.....	50
5. Conclusion & Outlook	55
6. Acknowledgments	56

Appendix A	57
Appendix B	59
Bibliography	61

1. INTRODUCTION

1.1 Quantum Computation

In 1983, legendary CalTech physicist and Nobel Prize laureate Richard Feynman gave a series of lectures on computing listed in the CalTech record as “Potentialities and Limitations of Computing Machines”. This was one of the earliest predictions that a quantum mechanical system could potentially outperform a classical system in certain computational tasks [1].

During the next two decades, important theoretical breakthroughs in quantum computation such as the development of efficient quantum algorithms and quantum error-correcting codes [2], lead to a concrete idea of the quantum computer. It turned out that systems and algorithms that exploit quantum mechanical effects could theoretically achieve exponential speed-up over their classical counterparts in certain problems, such as factoring integers [3] and estimating Gauss sums [4], or quadratic speed-up in problems such as searching unordered lists [5].

Except the theoretical innovations in the field of quantum computation, another factor that contributed positively in the rapid development of the field of quantum computing is the transistor size limitation introduced by quantum physics. The famous Moore’s law states that the number of transistors on an integrated circuit doubles approximately every two years [6]. Such a progression will soon be impossible as transistors are reaching the size of individual atoms and source-to-drain leakage currents due to quantum mechanical tunneling are dominating the gate currents. This fundamental limit on the size of transistors will also set an upper limit on the processing power a classical computer can have, thus making the quantum based computing systems, that do not experience such limitations, very attractive.

1.2 Spin as a Qubit

One approach of building a quantum computer is adapting valuable quantum properties in classical computing systems [7]. For example, by using the two degrees of freedom the spin of an electron has as a carrier of classical bits. This unit of quantum information is called quantum bit or qubit, the quantum analogue of the classical bit.

The simplest picture of the quantum mechanical spin is a magnetic moment, unique for each particle, that points up (state 0) or down (state 1) relative to a reference (usually an applied magnetic field) [8]. However, unlike a classical two-level system that can either be on state 0 or state 1, a quantum mechanical spin can be on an arbitrary superposition of these states. Using the Dirac notation, the two quantum states can be expressed as $|0\rangle$ and $|1\rangle$ and for their superpositioned state holds:

$$|\psi\rangle = \alpha|0\rangle + \beta|1\rangle \tag{1.1}$$

where α and β are the probability coefficients of states 0 and 1, respectively. The probability of measuring a specific state is given by the square of the absolute value of its probability coefficient. And since the particle can only be in one of the two states, it holds:

$$|\alpha|^2 + |\beta|^2 = 1 \quad (1.2)$$

This probabilistic behavior of a quantum system is due to the collapse of the otherwise deterministic Schrödinger wave function of the particle upon measurement: the particle is forced in one of the two states each time a measurement is taking place, thus making the measurement outcome non-deterministic (observer effect) [9].

The practical importance of the superposition property becomes apparent when comparing a qubit to a classical bit. A one-bit classical computer, in order to determine a function f of two possible input states 0 and 1, needs to evaluate the function twice, once for each individual state. Instead, a one-qubit quantum computer can use the linear superposition (1.1) as an input and thus evaluate the function only once. This property also scales for higher order-qubit quantum computers, consequently making the computing power of a quantum computer to scale exponentially with the number of qubits, while the computing power of their classical counterparts scales only linearly with the number of classical bits. Of course, the final outcome of a quantum computation can not be a superposition of states, since superposition exists only before it is measured. Nevertheless, by designing the logic operations accordingly, the superposition principle can still be taken advantage of to speed-up calculations [7].

Although the origin of macroscopic phenomena such as magnetization is quantum mechanical, these collective variables behave entirely classically. The quantum state of a magnetization vector for example, dephases so rapidly that superposition between vectors can not be observed. Only in systems with a small number of particles, and thus number of spins (for instance magnetic metallic molecules), quantum effects are observable in the behavior of their collective magnetization. Although superposition of spins has been observed in particle ensembles very early, only in recent years systems have been realized where individual electrons can be trapped and their quantum properties can be used as carriers of classical information [10]. Such a system was initially proposed by Loss and DiVincenzo in 1997 [11]. Their proposal suggested using the orientation of the spin of a single electron trapped in a semiconductor quantum dot as a quantum bit. The charge degrees of freedom of electrons in QDs have also been considered as a quantum bit, but such a system would arguably be too sensitive to electrical field noise to be practical [12]. In theory, any two-level physical system can be used as a qubit, but the system proposed by Loss and DiVincenzo has received considerable attention mostly due to its commonality with classical electronics [24].

It is worth noting that such a system merely uses quantum properties to improve the performance of classical computations. A true quantum computer would theoretically exploit the unique features of quantum mechanics to perform

computations that are intractable for systems based on classical logic, such as the simulation of complex quantum systems [1].

1.3 Quantum Dots

The technological drive to make electronic devices smaller and the continuously improved fabrication processes have some interesting scientific consequences. For instance, it is now routinely possible to define electron “boxes” in semiconductor devices that can confine any number of conduction electrons [10]. These three-dimensional structures have a side length smaller than the Fermi length of a typical electron. Therefore, an electron trapped inside such a structure will be confined in all three directions and will exhibit energy quantization in all three spatial dimensions, making the eigenenergies inside the structure discrete. This makes for an effectively zero-dimensional system called a quantum dot [13]. Recently, it has been demonstrated that electron holes (or simply “holes”) can also be confined inside a quantum dot.

Quantum dots consist of 10^3 to 10^9 atoms with an equivalent number of electrons. In semiconductors, all electrons are tightly bound to the nuclei except for a small fraction of conduction electrons. This small fraction can be varied from a single free electron to a several thousands free electrons by attaching a gate to the quantum dot and applying a voltage. Due to the three dimensional confinement of the electrons and the resulting quantized energy spectrum, quantum dots are often regarded as artificial atoms [14].

Quantum dots can also be operated as transistors via a field-effect gate. These devices are named single-electron transistors (SETs) and are reminiscent of the classical MOSFET, but instead of the usual inversion channel, a quantum dot acting as a conducting island, referred to as a Coulomb island, is embedded between the source and drain electrodes [15]. A more detailed account of single-electron transistors will follow on the next chapter.

There is a number of methods for defining quantum dots in semiconductors. In the past, colloidal synthesis [16], plasma synthesis [17], self-assembled fabrication [18], semiconductor lateral [19] and vertical dot [15] assembly, and even viral assembly [20] have been demonstrated.

For this study, quantum dots are electrostatically defined in semiconducting material. Silicon isotope materials have long electron spin coherence times because of their weak spin-orbit coupling and the predominance of nuclei with zero intrinsic angular momentum [2], making them ideal hosts for quantum dots. Individual quantum dots are created from two-dimensional electron and hole gases electrostatically induced at a Si/SiO₂ interface, referred to as 2DEG and 2DHG, respectively. The electrons and the holes are confined in the interface so they can only move laterally in a two dimensional plane, effectively creating the two-dimensional gas. Then, by employing electric gates, a small area of decreased potential is imposed in the 2DEG and a small area of increased potential is imposed in the 2DHG. Once the potential is applied, it is energetically favorable for the carriers

to remain confined in the area defined by the change of potential, thus creating depleted regions inside the gas. As 2DEG and 2DHG reservoirs, n, and p doped source and drain regions are used, respectively. The electrostatic potential of the quantum dot relative to the reservoirs is tuned by a gate electrode (often called a plunger) which controls the charge occupancy of the dot, permitting its operation as a single-charge transistor [21]. Electron-beam lithography (EBL) allows the fabrication of these gate structures with dimensions down to a few tens of nanometers, thus yielding very precise control over the size and the charge occupancy of the dot [10].

1.4 Charge Sensing

Charge sensing is an essential experimental tool since it allows the confirmation of electron or hole confinement inside a quantum dot down to the single charge level and the readout of the charge spin state, a useful property for quantum computation [22]. Identifying the charge occupancy is also possible by measuring the electrical transport through the dot via attached probes, but at low charge numbers measuring currents becomes challenging [23]. Charge sensing is a non-invasive process that is based on the fact that structures such as single-charge transistors and quantum point contacts possess high transconductance, making them sensitive to their local electrostatic environment and therefore excellent charge sensors [22]. It has been demonstrated that single-charge transistors exhibit the highest sensitivity amongst the two. For this study, a single-charge transistor acting as a charge sensor is co-fabricated across a quantum dot. Any small charge displacement in the SET due to its capacitive coupling to the quantum dot can then lead to a significant change in the SET current which then can be measured via attached probes [24].

1.5 Outline of the Thesis

This thesis describes a series of experiments aimed to characterize the single-charge transport in electrostatically defined quantum dots. Chapter 2 gives a brief introduction to the theoretical aspects of this thesis. We start with a few basic concepts of quantum mechanics, proceed with the discussion of the Coulomb blockade effect, and then we introduce a model that describes the transport in single quantum dots. At the end of the second chapter this discussion is repeated for double quantum dots. In chapter 3, we elaborate on the design of the devices, briefly discuss their fabrication process, and finally we give an introduction to the set-up used to carry out the experiments. In chapter 4 we report on the experiments performed on the single-charge devices. Finally, in chapter 5, we conclude this report by summarizing our experimental results and suggesting a future outlook.

2.1 Tunneling Through a Potential Barrier

In the first chapter, the concept of a quantum dot was introduced. An aspect that was not discussed, is the mechanism that connects this nanoscopic object with electrical leads in order to form electronic devices such as single-electron transistors. A schematic picture of a lateral quantum dot is shown in figure 2.1. As it can be seen, the quantum dot is separated from the source and the drain leads (this is usually done by an insulating material). Although the leads do not contact the quantum dot, electric current can still pass through the gap if the separation is sufficient small. This “connection” is achieved through the process of quantum tunneling [13].

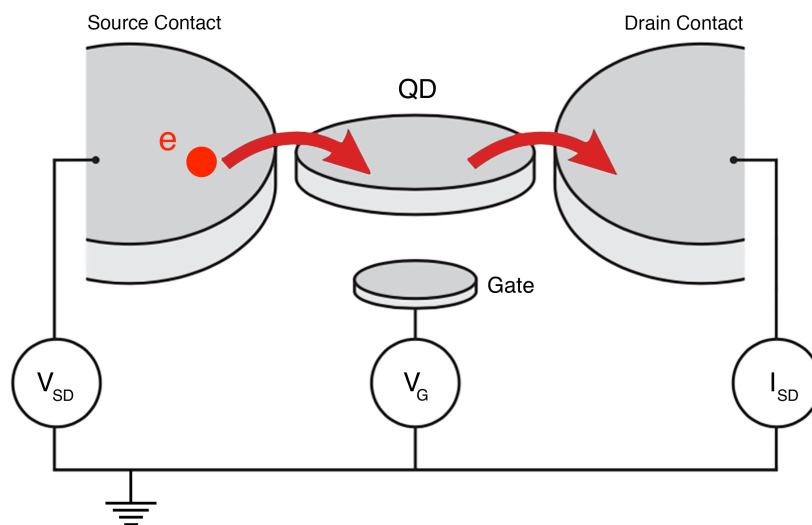


Figure 2.1: Schematic of a lateral quantum dot. The dot is coupled to the source and drain contacts via tunnel barriers. The red arrows represent tunneling events and thus current flow. Figure adapted from [10].

To investigate this phenomenon, the gap between the leads and the dot will be modeled as a potential energy barrier with height V_0 . According to classical physics, a particle of energy E , less than the height V_0 of the barrier, can not penetrate it. This makes the region inside the barrier classically forbidden (see figure 2.2). But due to the wave-particle duality, if the particle in question is one of the elementary particles, it should exhibit the properties of not only a particle, but also of a matter wave. The wave function associated with this particle must be continuous at the barrier and show an exponential decay inside it. The wave function must also be continuous on the other side of the barrier. Therefore, there is a finite probability that the particle will tunnel through the classically forbidden region. Since the energy conservation principle holds, after tunneling the particle will have the same amount of energy as before the tunneling event [9].

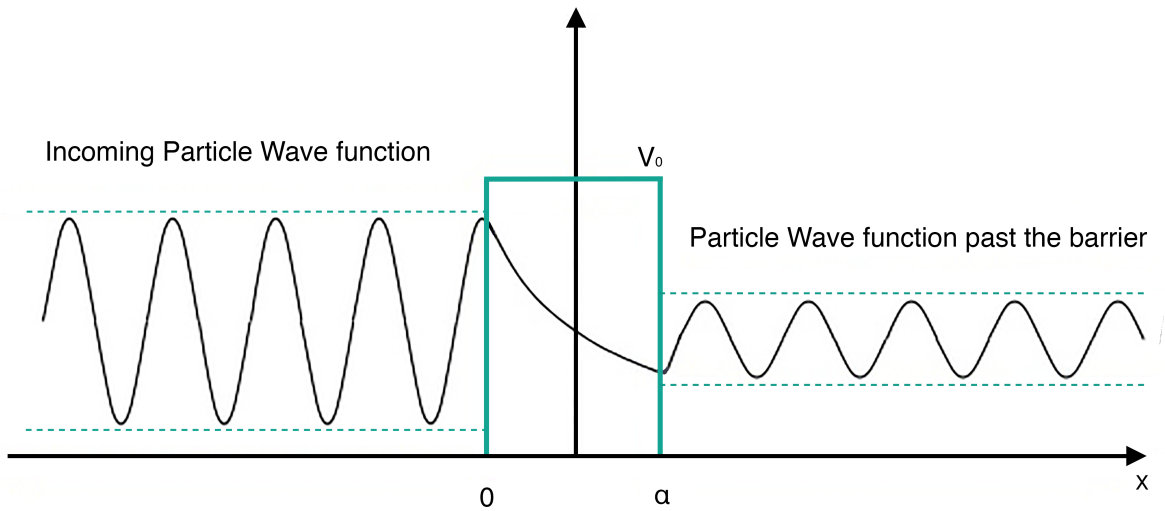


Figure 2.2: Particle wave function inside a classically forbidden potential barrier. On the right side of the barrier the probability of finding the particle reduces, while its energy remains constant on either side of the barrier.

The likelihood that the particle will tunnel through the barrier is given by the tunneling probability. Solving the Schrödinger wave-equation allows this probability to be calculated as [13]:

$$T = \frac{4E(E-V_0)}{V_0^2 \sin^2(k_2 a) + 4E(E-V_0)} \quad (2.1)$$

where

$$k_2 = \sqrt{\frac{2m(E-V_0)}{\hbar^2}} \quad (2.2)$$

and a , the width of the potential barrier V_0 (see figure 2.2).

Plotting the tunneling probability results in figure 2.3. The line on the left end of the plot shows the behavior of the particle for $E \ll V_0$, while the line on its right end, the behavior of the particle for $E \gg V_0$. In both cases, the particle is behaving classically. In between the two extremes, the quantum mechanical result is shown. Evidently, for $E < V_0$ there is some non-zero exponential probability the particle will be tunneled across the barrier. Also, for $E = V_0$, we have $T \approx 1$. For larger energies the tunneling probability is high, but there is also a finite probability that the particle will not be tunneled through the barrier but get reflected by it.

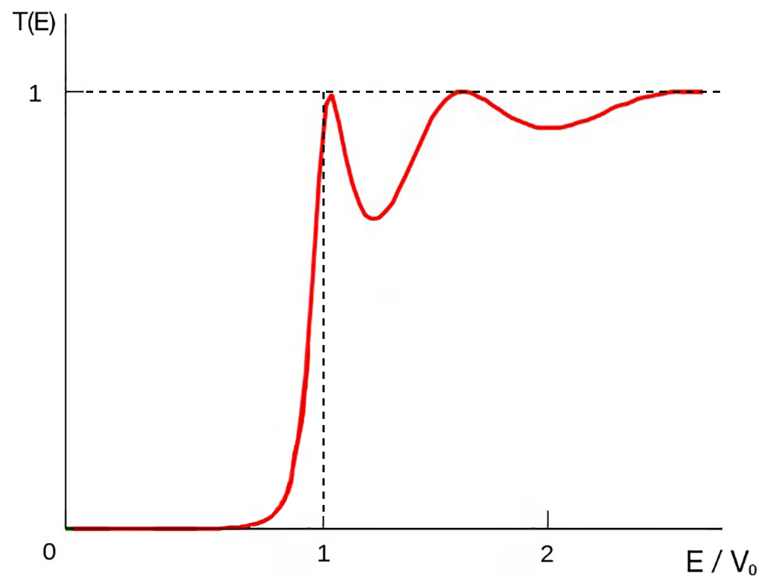


Figure 2.3: Tunneling Probability versus Energy for a potential energy barrier

2.2 Heisenberg Uncertainty Principle

Another important concept of quantum mechanics that will be proved useful as the discussion of quantum dots progresses, is that of the Heisenberg uncertainty principle. Introduced in 1927 by Werner Heisenberg, it states that the more precisely determined a particle's position is, the less precisely determined its momentum and vice versa [9].

If a wave consists only of a short pulse, such that it can be located inside an infinitesimal region Δx , then this wave-packet can be described by using the superposition of several plane waves. By adding more waves, this wave-packet becomes increasingly localized. A wave-packet can be separated into its individual plane waves by using a Fourier transformation. Each wave is characterized by a wave number k . The wave-packet confined in region Δx must therefore contain a range of different wave numbers Δk . One of the most important theorems of Fourier analysis states that those two ranges must follow the relationship: $\Delta x \Delta k \geq 1/2$. Since it is the result of calculus, this relationship holds for every wave encountered in nature and it is not restricted to quantum mechanical systems.

In quantum physics, the de Broglie wavelength formula associates a wavelength with the momentum of a massive particle through the plank constant h : $\lambda = \frac{h}{p} = \frac{2\pi\hbar}{p}$. Also, for every wavelength holds: $\lambda = 2\pi/k$. Combining the two relations and solving for two values of the momentum results in: $\Delta p = \hbar\Delta k$. Finally, if we combine this result with the Fourier analysis equation obtained earlier:

$$\Delta p \Delta x \geq \frac{\hbar}{2} \quad (2.3)$$

Which is the famous Heisenberg uncertainty principle. Once it was theorized that all particles also behave like waves, the uncertainty principle was merely a mathematical consequence. As it has been discussed, a form of the uncertainty principle is inherent in the properties of all waves. It arises in quantum mechanics simply due to the matter wave nature of all quantum objects and it is not related to the observer effect and the wave-function collapse discussed in the introduction.

2.3 Coulomb Blockade

As described in the first paragraph, the current flows from lead to lead through the quantum dot via a process called tunneling. In this type of situation, the quantum dot is acting as a conducting island, referred to as a quantum or Coulomb island. In order to model the quantum dot and its exterior leads, the classical concept of capacitance is used, resulting on a mixed classical-quantum model [13].

First, a simple model of two conductors separated by an insulating material will be considered. The space between the conductors will exhibit a capacitance C proportional to:

$$C = \frac{Q}{V} \quad (2.4)$$

Where Q is the net charge of the conductors, and V is the d.c. voltage between the two conductors. The electrostatic energy stored between them is given by:

$$E = \int_0^V Q dV = \int_0^V CV dV = \frac{1}{2} CV^2 = \frac{Q^2}{2C} = \frac{(ne)^2}{2C} = \frac{e^2}{2C} \quad (2.5)$$

Where n is the number of electrons between the conductors (we assume that a single electron is trapped) and e , the electron charge.

This energy is known as the Coulomb charging energy or simply charging energy and it is the energy required to add charge to one of the conductors.

For both conductors, the charging energy becomes:

$$E_C = \frac{e^2}{C} \quad (2.6)$$

This energy surpasses further electron transfer between the leads, unless it is overcome by either thermal excitations or by an external bias voltage. This suppression of electron transport is termed Coulomb blockade of tunneling, or simply Coulomb blockade, named after Charles-Augustin de Coulomb's electrical force [25].

For a simple capacitor formed by two parallel conducting plates of area A and plate separation d , the capacitance of the configuration is given by:

$$C = \frac{\epsilon A}{d} \quad (2.7)$$

Where ϵ is the electric constant.

Therefore, for plates with nanoscale dimensions, the small values of capacitance will lead to a considerable change in the Coulomb charging energy. While in macro-sized circuits, because the area of the capacitor plates is very large, no Coulomb Blockade effects can be observed [13].

2.4 Tunnel Junctions

In order to include the tunneling events in a lumped element model, the transport taking place across the tunneling barrier is modeled as a leaky capacitor. This is, a capacitor with a small d.c. current (leaky current) flowing from one plate to the other when a d.c. voltage is applied across it. The leaky capacitor is modelled as an ideal capacitor with a resistor in parallel (left side of figure 2.4). Every time a voltage is applied to the resistor-capacitors terminals, a current starts to flow across the resistor. This leaky current essentially models the current due to tunneling. Thus, the resistor across the ideal capacitor is often regarded as a tunnel resistor. The parallel combination of the capacitor and the resistor is termed tunnel junction (right side of figure 2.4) and it will be used in the proceeding quantum dot circuit models to model tunneling events.

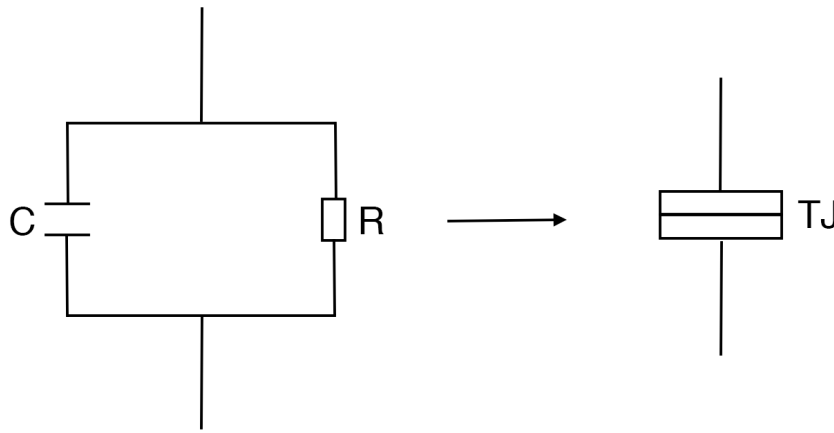


Figure 2.4: left side: leaky capacitor model consisting of an ideal capacitor and resistor in parallel. Right side: tunnel junction model.

2.5 Requirements for Coulomb Blockade

Returning to a previous statement, to establish the Coulomb blockade, the charging energy must be greater than the thermal energy. This can be expressed as follows:

$$E_C = \frac{e^2}{2C} \gg \frac{1}{2}k_B T \Rightarrow \frac{e^2}{C} \gg k_B T \quad (2.8)$$

Where k_B is the Boltzmann constant and T , the temperature.

Recalling relation (2.7), it can be seen that the requirement expressed in (2.8) can be met by making the dot sufficiently small. This temperature constraint is also the reason all single-electron devices in this study are strictly operated at cryogenic temperatures.

Moreover, the tunneling resistance considered in the previous paragraph must be sufficiently large to not allow the delocalization of the charge in the capacitor plates, but at the same time, sufficient small to allow the tunneling current to flow through the capacitor [13]. This can be expressed by using the Heisenberg

uncertainty relation discussed earlier: $\Delta p \Delta x \geq \frac{\hbar}{2}$ from which it can be derived that:

$$\Delta(\hbar k) \Delta x = \Delta\left(\hbar \frac{\omega}{c}\right) \Delta x = \Delta(\hbar \omega) \Delta t = \Delta E \Delta t \geq \frac{\hbar}{2} \quad (2.9)$$

In addition to that, the time between the tunneling events is considered equal to the approximate lifetime of the electron energy state on one side of the barrier. This time is also identical to the time constant of a parallel RC circuit:

$$\tau = RC \quad (2.10)$$

By combining (2.9) and (2.10), the uncertainty in energy is derived:

$$\Delta E \geq \frac{\hbar}{2RC} \quad (2.11)$$

And to observe the Coulomb Blockade effect, the energy in (2.5) must be larger than this energy uncertainty, thus making:

$$R \gg \frac{\hbar}{e^2} \approx 4.1 \text{ K}\Omega \quad (2.12)$$

This requirement can be met by weakly coupling the dot to the source and drain leads.

2.6 Single Quantum Dot Circuit Model

Now that the theory behind tunneling and tunneling junctions has been addressed, the equivalent circuit for a quantum dot coupled to source and drain terminals and excited by a voltage source can be attained. By definition, these terminals are large and thus contain much more electrons (or holes) than the quantum dot. For this reason, the source and drain terminals are regarded as charge reservoirs. The potential profiles for electron and hole quantum dots are shown in figure 2.5. The voltage source applies a potential difference that essentially “empties” those charge reservoirs. A third terminal that provides capacitive coupling is used as a gate terminal, effectively creating a single-charge transistor device. As in a traditional MOSFET, this contact is intended to control the flow of charges across the source-drain channel and does not inject charges directly. The equivalent circuit is shown in figure 2.6, where the constant interaction (CI) model has been used to model the Coulomb interactions in the system [19]. A quantum dot occupied by holes behaves similarly to one occupied by electrons. Therefore, for simplicity, the following discussion will be restricted to electrons.

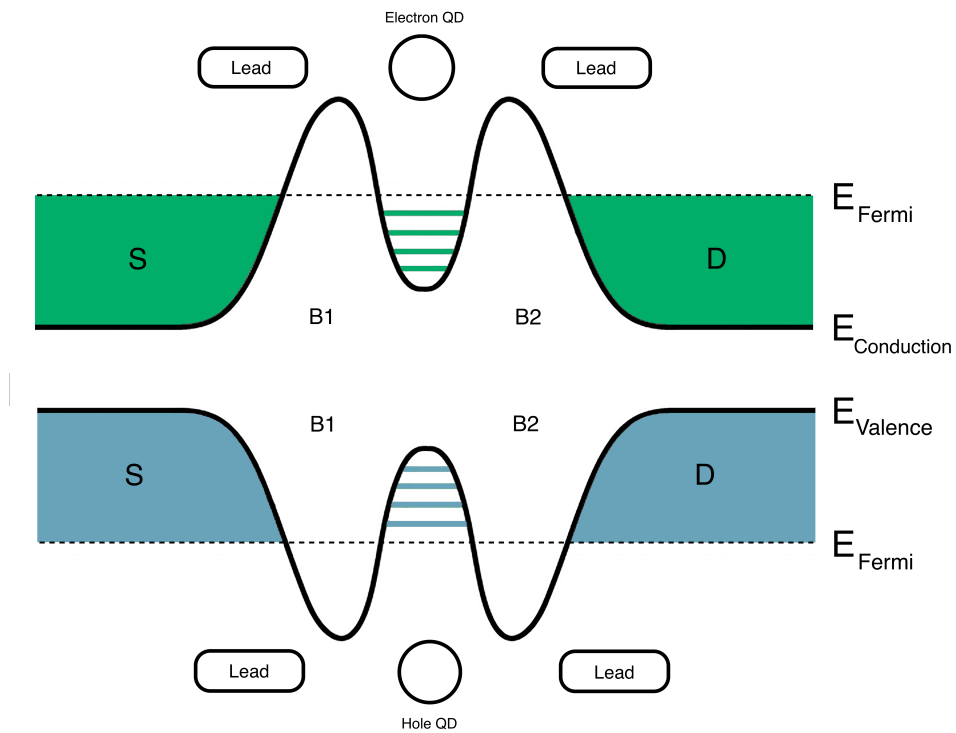


Figure 2.5: Top: Potential profile of an electrostatically defined electron quantum dot. Bottom: Potential profile of an electrostatically defined hole quantum dot. The confinement of the charge carriers results in discrete energy levels inside the dots.

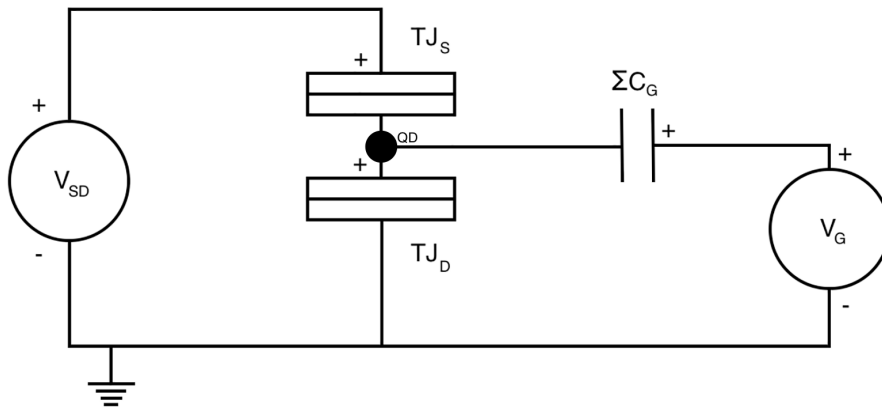


Figure 2.6: Circuit model of a single-electron transistor. TJ_{S} has a resistance value of R_{S} and a capacitance value of C_{S} . Accordingly, TJ_{D} has a resistance value of R_{D} and a capacitance value of C_{D} . The two voltage sources determine the position of the discrete energy levels inside the dot.

The CI model makes two assumptions about the system. First, it is assumed that the discrete quantum energy levels of the dot can be described independently of the number of electrons inside it. Second, all coulombic interactions amongst the electrons confined inside the dot and between these electrons and the electrons in different locations inside the system (e.g.: in the source and drain leads) are parametrized by a single capacitance C , which is the sum of the capacitances between the dot and the source (C_s), the drain (C_D), and the gates ($\sum C_G$):

$$C = C_s + C_D + \sum C_G \quad (2.13)$$

Under these assumptions, the total energy of a quantum dot containing N electrons can be calculated. The total energy will consist of an electrostatic term and a quantum mechanical term. The electrostatic term is equal to the energy stored inside an ideal capacitor:

$$E_{electrostatic} = \frac{1}{2} \frac{Q^2}{C} \quad (2.14)$$

Where the charge Q is the charge inside the quantum dot and it is comprised of three terms, the charge induced by the source-drain bias, $C_s V_{SD}$, the charge induced by the gate voltage, $C_G V_G$, as well as the charge due to the self-capacitance of the quantum dot, $-|e| (N - N_0)$, where e is the elementary charge, N is the number of electrons in ground state, and N_0 , the number of electrons at zero gate voltage. The charge terms $C_s V_{SD}$ and $C_G V_G$ can change continuously since this energy term is classical in nature.

Thus, (2.14) becomes:

$$E_{electrostatic} = \frac{[-|e| (N - N_0) + C_s V_{SD} + C_G V_G]^2}{2C} \quad (2.15)$$

The drain capacitor is assumed to be connected at zero potential (see figure 2.6), hence the factor C_s doesn't appear in the energy term. Now, the discrete energy spectrum of the quantum dot is taken into account and an additional term that represents the summation over the occupied quantized orbital energies on the dot that are separated by $\Delta E_n = E_n - E_{n-1}$ will emerge:

$$E_{quantum} = \sum_{n=1}^N E_n \quad (2.16)$$

Finally, the total energy of the quantum dot will be given by the sum of these two terms:

$$U(N) = \frac{[-|e| (N - N_0) + C_s V_{SD} + C_G V_G]^2}{2C} + \sum_{n=1}^N E_n \quad (2.17)$$

2.7 Charge Transport in Quantum Dots

The simple model we just presented, allows us to derive an expression for the electrochemical potential that it would have otherwise been very cumbersome to calculate. The electrochemical potential is defined [7] as the energy required to add the N^{th} electron to the dot (or alternatively, the transition between the N and $N-1$ electron state):

$$\mu(N) = U(N) - U(N - 1) \quad (2.18)$$

And by substituting (2.17), it is obtained that:

$$\mu(N) = \left(N - N_0 - \frac{1}{2}\right) E_C - \frac{E_C}{|e|} (C_S V_{SD} + C_G V_G) + E_N \quad (2.19)$$

Where $E_C = \frac{e^2}{C}$ is the charging energy defined earlier.

Another energy concept of high relevance is the addition energy. The addition energy is the energy required to change the number of electrons inside the dot discretely. It is defined as:

$$E_{\text{addition}}(N) = \mu(N + 1) - \mu(N) = E_C + (E_{N+1} - E_N) = E_C + \Delta E \quad (2.20)$$

It is equal to the separation distance between two adjacent energy levels with specific electrochemical potentials (see figure 2.7 A) and it consists of two terms, the charging energy E_C (a purely electrostatic term) and the energy spacing between two discrete quantum energy levels (or orbital energy), ΔE . For a classical dot without a quantized orbital energy spectrum (a Coulomb island), ΔE is evidently zero. Furthermore, ΔE can also be zero when two electrons are added to the same spin-degenerate level (same orbital). The addition energy also equals to the peak spacing in a conductance versus gate voltage plot (see figure 2.8). It is important to note that this plot depicts the conductance of a classical dot (a charge island with high density of states) since it exhibits regularly spaced Coulomb peaks. In the case of a quantum dot, irregularly spaced Coulomb peaks are expected due to the additional orbital energy term, which unlike the charging energy term, it is not constant. The dependence of the addition energy on the orbital energy in a quantum dot justifies the term “artificial atom” that was ascribed to them during the introduction. The conducting islands in single-electron devices exhibit a behavior similar to a classical dot.

Charge tunneling events through the dot depend on the alignment of the electrochemical potentials on the dot with respect to the electrochemical potentials of the source and the drain. By applying a bias voltage V_{SD} (defined as $V_S - V_D$ but in the model presented earlier, V_D is connected to the ground and thus equals to zero, effectively providing what is called an asymmetric bias) between the source and drain reservoirs, an energy window between the electrochemical potentials of the source and the drain opens up. This window is termed bias window and its size is related to the electrochemical potentials of the leads by: $\mu_S - \mu_D = eV_{SD}$ [26]. The bias window

translates into a height difference between the electrochemical potential levels of the the source and the drain (see figure 2.7 B). If there is an empty electrochemical potential level in the dot within the bias window, charges can tunnel from the occupied states of the one reservoir onto the dot and then from the dot off to the empty states in the other reservoir. We will first consider the low bias regime where the bias window is by definition sufficiently large for only first-order tunneling events to take place [7]. This is, an electron tunnels first from one reservoir onto the dot and then from the dot to the other reservoir (as in figure 2.7 C). Therefore, at no point more than one electrons can occupy the dot at the same time. If there is no empty electrochemical potential level within the bias window, no tunneling event can take place and thus, the number of electrons on the dot will remain fixed and no current will flow through it. This is known as the Coulomb blockade effect discussed earlier (see figures 2.7 A and 2.7 B).

As it can be seen from (2.19), the Coulomb blockade can be lifted by applying a gate voltage. A positive V_G will depress the charging energy gap due to the Coulomb blockade effect, thus allowing an empty electrochemical potential level in the dot to move within the bias window (see figure 2.7 C).

By sweeping the gate voltage and measuring the current flowing through the dot while keeping the bias voltage close to zero, a conductance versus gate voltage plot can be made (figure 2.8). At the positions of the conductance peaks, an electrochemical potential level inside the dot is aligned inside the bias window and a single-electron event takes place. This causes a current to flow, which then translates to a change in the conductance of the dot. In the valleys between the conductance peaks, the number of electrons on the dot is fixed due to the Coulomb blockade [10]. As mentioned earlier, the distance between the peaks corresponds to the addition energy.

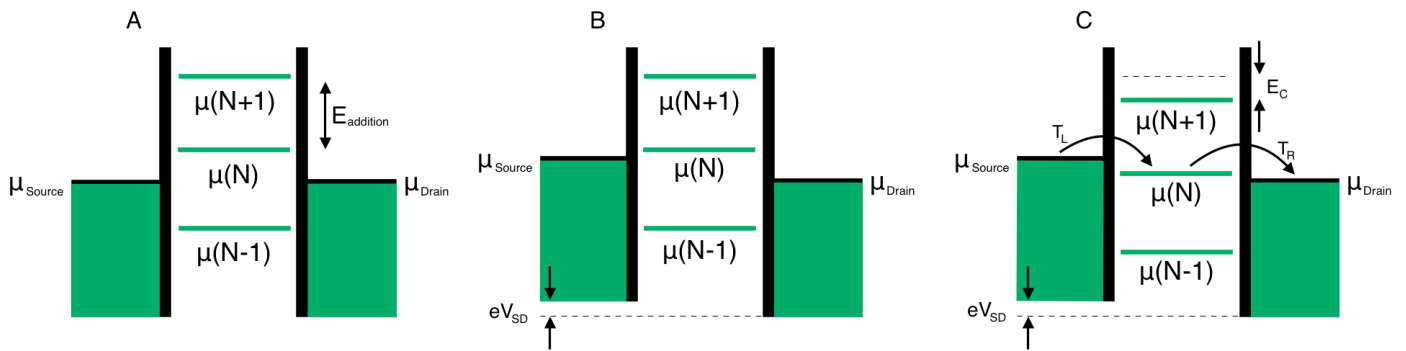


Figure 2.7: Schematic diagrams of the potential landscape of a quantum dot. In A, no electrochemical potential on the dot falls within the bias window. Therefore, the number of electrons is fixed at $N-1$ due to the Coulomb blockade effect. In B and C, the electrochemical potential on the leads depends on the bias voltage by $\mu_s - \mu_D = eV_{SD}$. In B, the electrochemical potential of the source is lifted due to the applied bias voltage and the bias window is widened. Nevertheless, the electrochemical potential for adding the N th electron to the dot still lies above the bias window and hence the Coulomb blockade remains. In C, the Coulomb blockade is depressed by applying a gate voltage equal to the charging energy (which should be equal to the addition energy for the low bias regime case). Now, the whole “ladder” of electrochemical potential levels on the dot is shifted down [7]. On each case, the electrochemical potential level for adding the next electron is separated from the previous potential level by the addition energy. The probability of each tunneling event depends on the mass and energy of the particle, and also the width and height of the potential barrier as it was defined in (2.1).

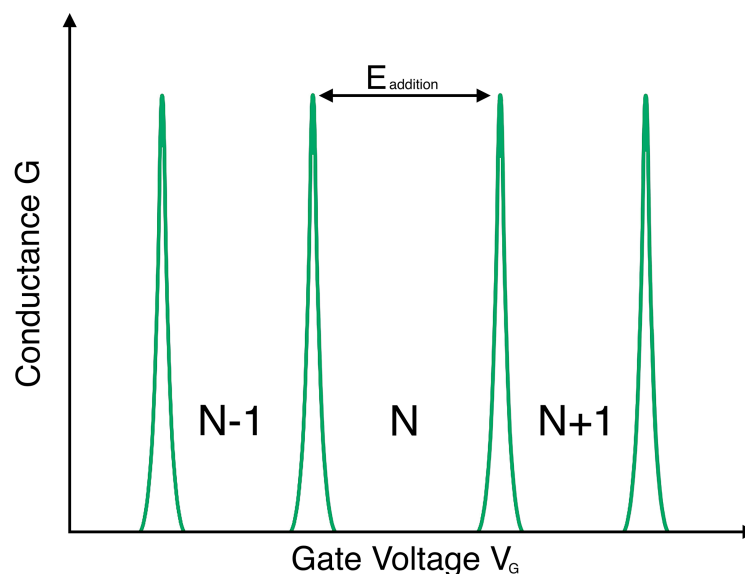


Figure 2.8: Coulomb peaks in Conductance versus Gate Voltage on a charge island with high density of states for zero bias voltage. Each peak corresponds to a situation similar to figure 2.7C (but for no applied bias), while each valley to the Coulomb Blockade situation depicted in figure 2.7A. The addition energy on this island is equal to only the charging energy, hence the regularly spaced Coulomb peaks.

2.8 Stability Diagrams in the Low-Bias Regime

By measuring the current through the dot while sweeping the bias voltage for different values of the gate voltage, a source-drain bias voltage versus gate voltage plot can be made (figure 2.9). The plot can also contain information about the differential conductance (the derivative of the current with respect to the source-drain bias), which is usually represented by a color gradient. This plot is often called a level spectroscopy diagram or a stability diagram and always exhibits a characteristic rhombic structure. Inside the diamond-shaped regions, the number of electrons on the dot is fixed due to the Coulomb blockade effect and no current can flow through them [7]. These regions are often called Coulomb diamonds. Each diamond corresponds to a fixed number of N electrons inside the dot. The points at the end of each diamond where the upper right and lower right edge of the diamond join along the gate voltage axis are called degeneracy points. At these points the energy of adding the N^{th} and the $N^{\text{th}+1^{\text{st}}}$ electron to the dot is the same (thus, the characterization “degenerate”). Outside the diamonds, the Coulomb blockade is lifted and single-electron tunneling events and thus current flow, take place. The edges of each diamond therefore signify the onset or the termination of a current flow. As we move to the right of the plot, there is a higher gate voltage and therefore the electrochemical potential “ladder” on the dot shifts down. Every time the edge of a diamond is reached, there is an alignment between one of the the electrochemical potential levels inside the dot and the electrochemical potential level of either the source (upper left and lower right diamond edges) or the drain (upper right and lower left diamond edges).

The shape of the Coulomb diamonds can be interpreted as follows: if we assume that the bias is applied symmetrically to the source and the drain reservoirs, we can derive two new relations for their electrochemical potential: $\mu_s = \mu_0 + eV_{SD}/2$ and $\mu_D = \mu_0 - eV_{SD}/2$, for the source and drain potentials, respectively. Where μ_0 is the potential of both the reservoirs for zero bias voltage (we assume that the reservoir potentials are aligned for $V_{SD} = 0$). From this we can derive a set of requirements for the electron configuration inside the dot to be stable. For a positive source-drain voltage, $V_{SD} > 0$, the following relations should hold: $\mu_N < \mu_0 - eV_{SD}/2$ and $\mu_{N+1} > \mu_0 + eV_{SD}/2$. Accordingly, for a negative source-drain voltage, $V_{SD} < 0$, it should hold that: $\mu_N < \mu_0 + eV_{SD}/2$ and $\mu_{N+1} > \mu_0 - eV_{SD}/2$. These inequalities when combined with (2.19) can then be translated into a set of equations that describe the Coulomb diamond edges, where the coulomb blockade is either lifted, or imposed. A detailed derivation of the so called borderline-equations can be found in [27]. By plotting these equations, we obtain the rhombic structure depicted in figure 2.9.

By definition, in the low-bias regime considered here, no excited states exist. Thus, unlike the high bias regime that will be discussed later, the area outside the diamonds is normally featureless. The height of each diamond corresponds to the addition energy, which for the low bias regime has only an electrostatic term. Therefore, the height of each diamond equals to the constant charging energy E_C . From the slope of each diamond the capacitance value of the capacitively coupled source, drain, and gate leads can be quantitatively determined.

Since the conducting islands in single-electron devices usually exhibit dense energy states, we can consider their energy spectrum as being continuous. Therefore, their addition energy has a finite electrostatic term and zero orbital energy, thus making their stability plots usually identical to those of quantum dots biased in the low-bias regime.

The Coulomb diamond structure has been observed in a variety of experiments on quantum dots. Spectroscopy diagrams are an invaluable tool for understanding the nature of single charge transport phenomena. They provide insight into the energy spectrum of the dot and allow the occupation number and the capacitive coupling of the dot to be determined by just looking at the diagram's features.

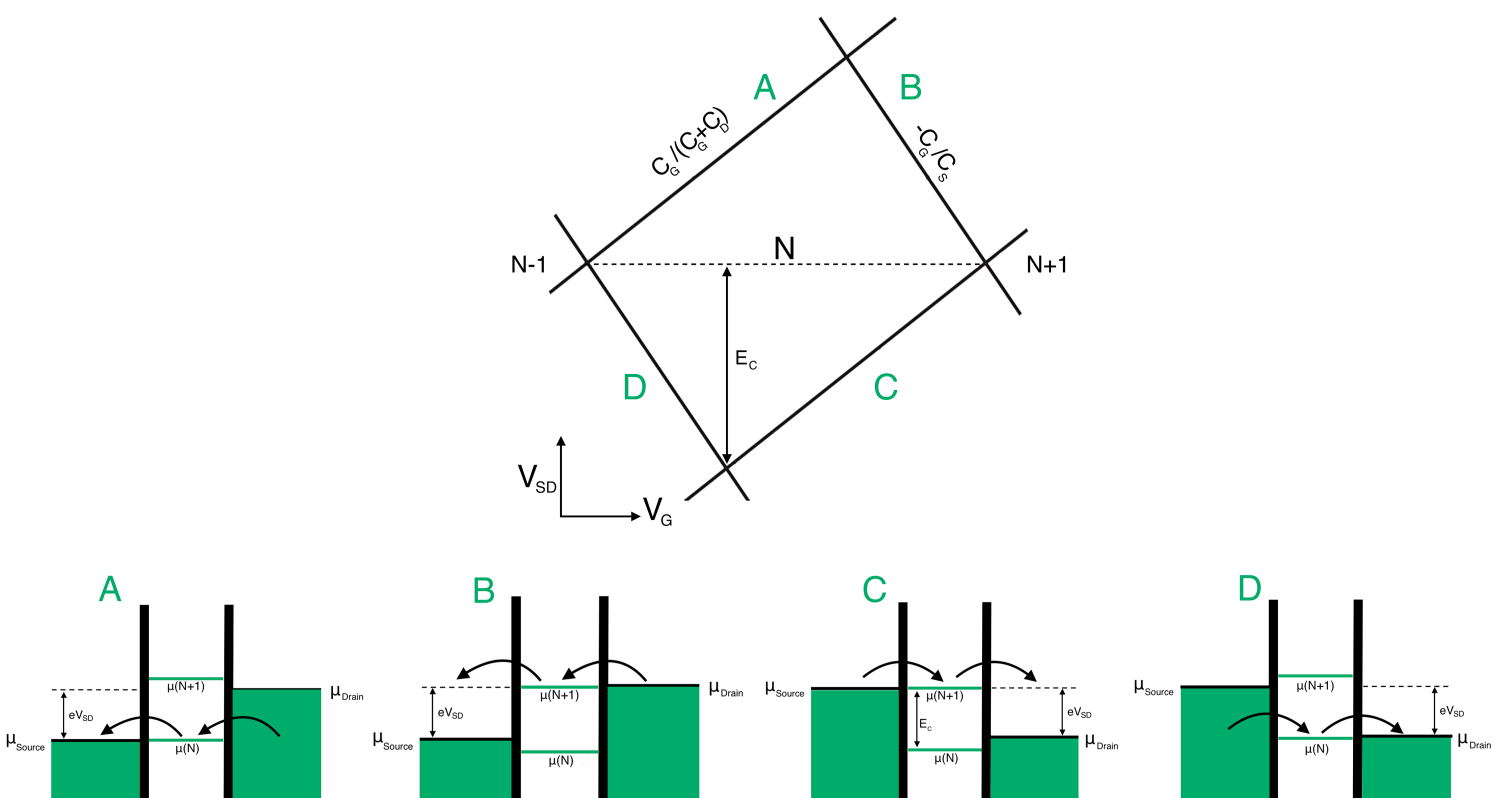


Figure 2.9: Coulomb diamonds in differential conductance for V_{SD} versus V_G in the low-bias regime. At the diamond edges, the electrochemical potential on the dot is aligned with either the source or the drain potential, corresponding to either the termination (left-hand side of the diamond) or onset (right-hand side of the diamond) of the tunneling current. Inside the diamond no transport is allowed due to the Coulomb blockade effect. By definition, only single-electron tunneling events take place in this low-biased regime.

2.9 Stability Diagrams in the High-Bias Regime

At the high bias regime, multiple dot energy levels can participate in the charge tunneling [10]. Every time an excited state level enters the (now widened) bias window together with an electrochemical potential level in the dot, an additional transport channel opens up allowing electrons to tunnel via one of the two levels (figure 2.10 A). Also, multiple tunneling events can take place at the same time if multiple electrochemical potentials are aligned inside the bias window (figure 2.10 B). The new transport channels due to the excited states appear in the stability diagram discussed earlier as lines emanating and running parallel to the diamond edges (see figure 2.11). Lines that end to the N^{th} Coulomb diamond correspond to excited states of the N^{th} electron and so on. In case of a double tunneling event of the e.g. N^{th} and $N^{\text{th}+1^{\text{st}}}$ electron, a new Coulomb diamond will appear between the old N^{th} and $N^{\text{th}+1^{\text{st}}}$ diamonds so its lower edges will be tangential with the upper right edge of the N^{th} diamond and the upper left edge of the $N^{\text{th}+1^{\text{st}}}$ diamond (see figure 2.11). For single - electron transport between non-excited dot potential levels, the edges of the diamond have the same behavior as in the low-bias regime (see figure 2.9). Furthermore, from the slope of each diamond the capacitance of the source, drain, and gate leads can be determined, just like in the low-bias case. The height of each diamond corresponds again to the addition energy and consequently, for a quantum dot with well-quantized energy levels, the non-constant orbital energy term ΔE will cause the Coulomb diamonds to have variations in height. It is important to mention that an excited state that enters the bias window can be due to multiple effects. Except the orbital excitations discussed here, it can be due to spin excitations, excitations due to Zeeman splitting or excitations due to lattice vibrations.

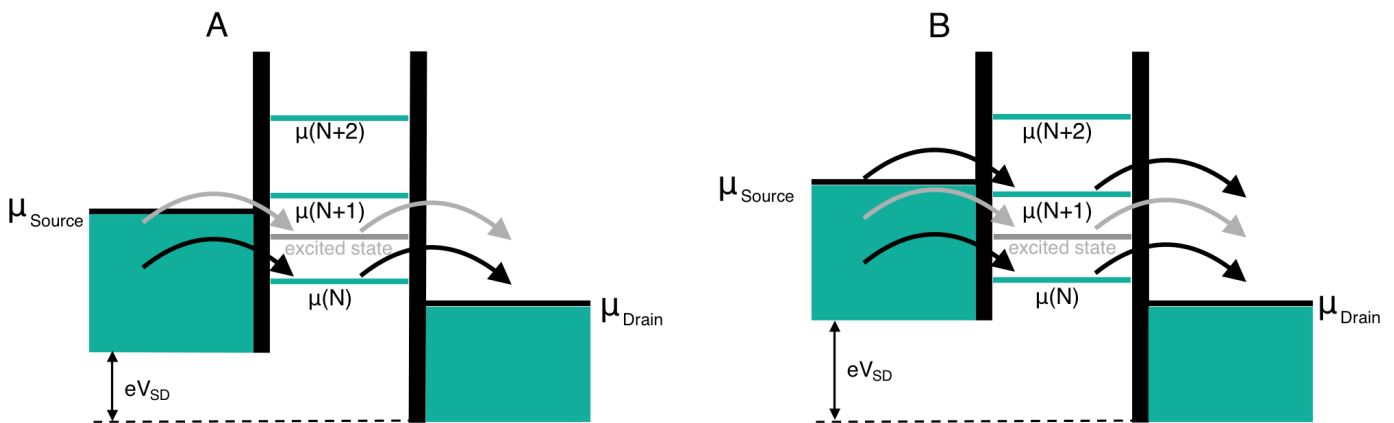


Figure 2.10: Schematic diagrams of the potential landscape of a quantum dot in the high-bias regime. In A, the excited state of the N^{th} electron aligns inside the bias window together with the electrochemical potential for adding the N^{th} electron to the dot. Electrons can now tunnel via one of the two available transport paths. The separation between these two levels equals to the orbital energy ΔE . In B, the bias window is sufficiently large for two electrochemical potential levels to be aligned within it, thus allowing a double-tunneling event to take place. In principle, any number of electrons can tunnel through the dot at the same time if the bias window is large enough and a corresponding number of potential levels is aligned inside it. The probability of each tunneling event is again given by (2.1).

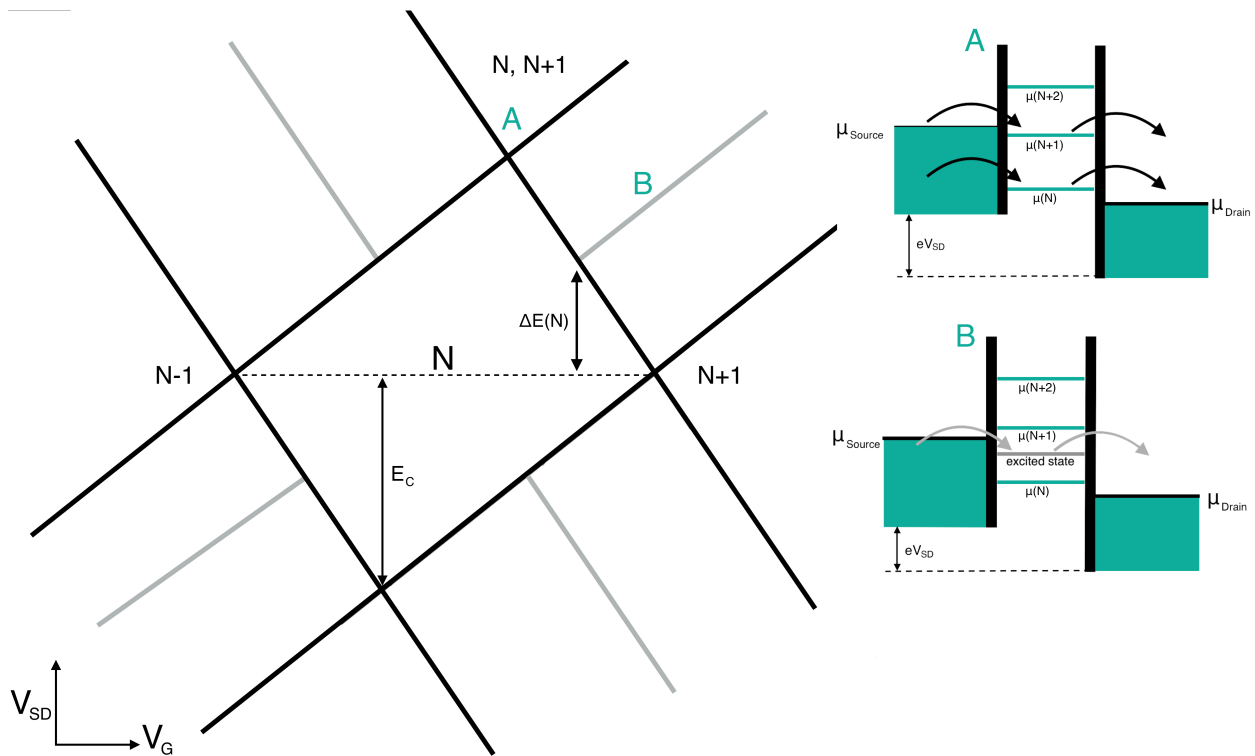


Figure 2.11: Coulomb diamonds in differential conductance for V_{SD} versus V_G in the high-bias regime. The transport between non-excited, single, dot potential levels appears as diamond edges in a fashion identical to that of the low-bias regime. The slope of each diamond edge depends again on the capacitance of the source, drain, and gate lead coupling. The gray lines indicate transport through excited states. Double-transport events appear as a new set of Coulomb diamonds running above the single-transport Coulomb diamonds.

2.10 Charge Transport in Double Quantum Dots

In a similar to a single quantum dot fashion, systems consisting of two coupled quantum dots can be fabricated. Where single quantum dots are regarded as artificial atoms, coupled double quantum dots can be considered as artificial molecules [28]. In that situation, electrons are not fully localized inside a single quantum dot, but occupy orbitals that span both quantum dots. Depending on the strength of the tunnel coupling between the dots, the two dots can form ionic-like or covalent-like bonds for weak or strong tunnel coupling, respectively. In this paragraph we focus on charge transport through lateral double quantum dots coupled in series. The potential profile for electron double quantum dots is shown in figure 2.12. The profile of hole double quantum dots is the horizontally mirrored profile of electron double quantum dots. It is important to notice the similarities between these potential profiles and the profiles of single quantum dots as shown in figure 2.5. It is important to notice the similarities between these potential profiles and the profiles of single quantum dots as shown in figure 2.5

By again employing the mixed classical-quantum model described in the previous sections together with the constant interaction (CI) model to model the Coulomb interactions, an equivalent circuit similar to that derived for single quantum dot circuits can be made for the case of double quantum dot circuits (figure 2.13).

The main difference between the two models is the presence of a second gate voltage source dedicated to the second quantum dot, and of a third tunnel junction that couples each dot to the other.

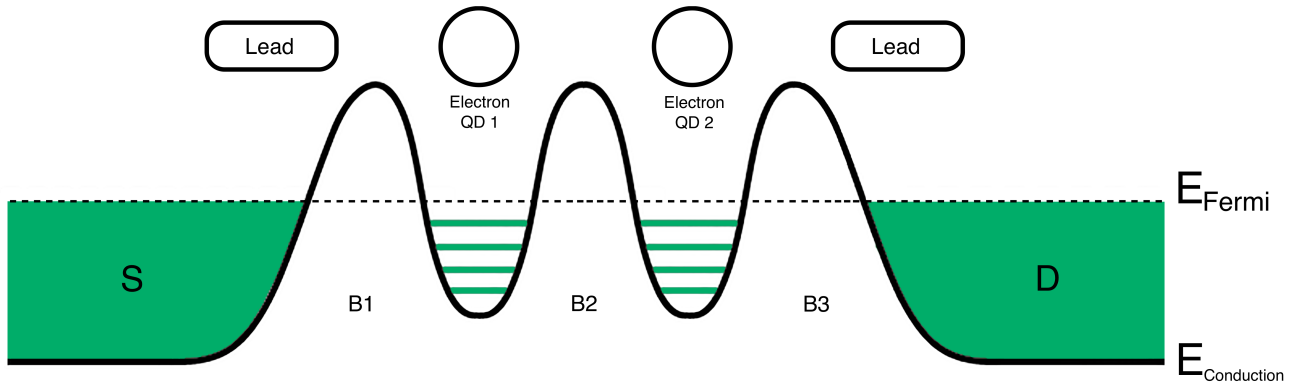


Figure 2.12: Potential profile of an electrostatically defined double electron quantum dot. The confinement of the electrons results in discrete energy levels inside the dots. If the second barrier is lowered sufficiently, one large quantum dot will be defined instead of two individual dots.

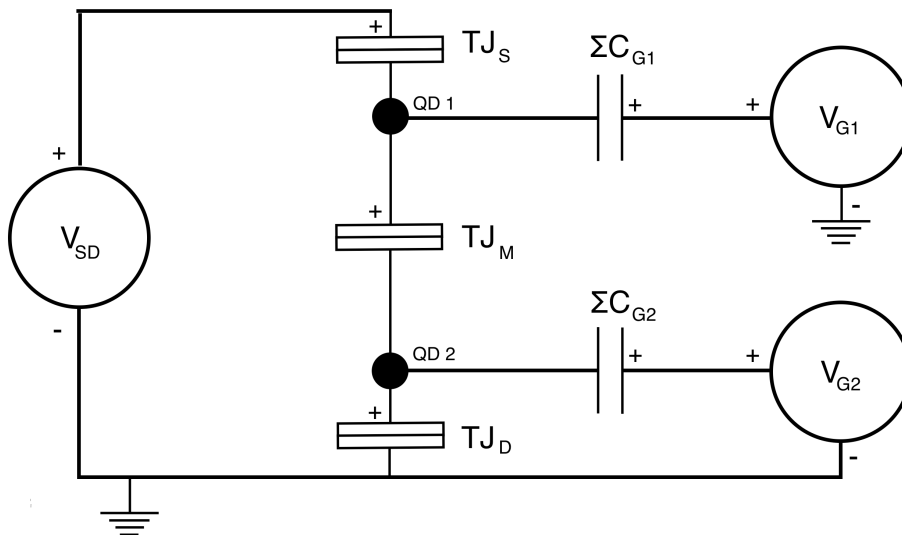


Figure 2.13: Circuit model of two coupled single electron-transistors. TJ_S has a resistance value of R_S and a capacitance value of C_S . Accordingly, TJ_D and TJ_M have a resistance value of R_D and R_M and a capacitance value of C_D and C_M , respectively. The voltage sources determine the position of the discrete energy levels inside the dots independently.

By following the assumptions of the CI model as described in paragraph 2.6, the Coulombic interactions of the electrons inside the system can be parameterized by two capacitance terms: C_1 and C_2 . C_1 is the sum of all the capacitances attached to the first dot:

$$C_1 = C_s + C_M + \sum C_{G1} \quad (2.21)$$

while C_2 is the sum of all capacitances attached to the second dot:

$$C_2 = C_D + C_M + \sum C_{G2} \quad (2.22)$$

If we now assume that the cross coupling between the two dots is weak, the C_M term becomes negligible. As a further assumption we take $V_{SD} = 0$, that is, only the linear transport regime is considered. Then, by following the same derivation as in for the single quantum dot circuit presented earlier, the total electrostatic energy of the double quantum dot circuit can be described by the sum of the electrostatic energies of two independent (uncoupled) quantum dots:

$$E_{electrostatic} = \frac{[-|e|(N_1 - N_{1,0}) + C_{G1}V_{G1}]^2}{2C_1} + \frac{[-|e|(N_2 - N_{2,0}) + C_{G2}V_{G2}]^2}{2C_2} \quad (2.23)$$

Where N_1 is the number of electrons in the ground state of the first quantum dot, N_2 the number of electrons in the ground state of the second dot, $N_{1,0}$ the number of electrons in the first dot for $V_{G1} = 0$, and $N_{2,0}$ the number of electrons in the second dot for $V_{G2} = 0$. Similar to what have been discussed before, if we now take into account the discrete energy spectrum of the quantum dots, an additional energy term for each individual dot that represents the summation over the occupied quantized orbital energy levels on it will emerge:

$$E_{quantum} = \sum_{n=1}^N E_n \quad (2.16)$$

The total energy of the two uncoupled quantum dots will then be given by:

$$U(N) = \frac{[-|e|(N_1 - N_{1,0}) + C_{G1}V_{G1}]^2}{2C_1} + \frac{[-|e|(N_2 - N_{2,0}) + C_{G2}V_{G2}]^2}{2C_2} + \sum_{n=1}^N E_{1,n} + \sum_{n=1}^N E_{2,n} \quad (2.24)$$

Furthermore, if we now take into account the cross-coupling effects, we can define the electrochemical potential as the energy required to add the N th electron to the first dot while keeping the number of electrons on the second dot constant, or vice-versa:

$$\begin{aligned} \mu_1(N_1, N_2) = U(N_1, N_2) - U(N_1 - 1, N_2) = & \left(N_1 - N_{1,0} - \frac{1}{2}\right) E_{C1} - \\ & \frac{1}{|e|} (C_{G1}V_{G1}E_{C1} + C_{G2}V_{G2}E_{CM}) + N_2 E_{CM} + E_{1,N} \end{aligned} \quad (2.25)$$

and also,

$$\begin{aligned} \mu_2(N_1, N_2) = U(N_1, N_2) - U(N_1, N_2 - 1) = & \left(N_2 - N_{2,0} - \frac{1}{2}\right) E_{C2} - \\ & \frac{1}{|e|} (C_{G2} V_{G2} E_{C2} + C_{G1} V_{G1} E_{CM}) + N_1 E_{CM} + E_{2,N} \end{aligned} \quad (2.26)$$

Where $E_C = \frac{e^2}{C}$ is the charging energy for each dot. A detailed derivation of these relations can be found in [28].

The addition energy discussed in paragraph 2.7 is now interpreted as the energy required to change the number of electrons inside one of the dots discretely, while keeping the number of electrons on the other dot constant. It holds:

$$\begin{aligned} E_{1,addition}(N_1, N_2) = \mu_1(N_1 + 1, N_2) - \mu_1(N_1, N_2) = & E_{C1} + \\ & (E_{1,N+1} - E_{1,N}) = E_{C1} + \Delta E_1 \end{aligned} \quad (2.27)$$

similarly,

$$\begin{aligned} E_{2,addition}(N_1, N_2) = \mu_2(N_1, N_2 + 1) - \mu_2(N_1, N_2) = & E_{C2} + \\ & (E_{2,N+1} - E_{2,N}) = E_{C2} + \Delta E_2 \end{aligned} \quad (2.28)$$

Now that the energies of the double dot system are defined, it is possible to plot stability diagrams akin to those discussed in sections 2.8 and 2.9. Plotting equations (2.27) and (2.28) for zero orbital energy will result in a description of the classical transport regime, reminiscent to the low-bias regime of the single quantum dots. The bias voltage is still considered to be zero (linear regime), hence, the electrochemical potential of the source and drain is also zero. This sets as a condition that the number of charges on the dots in equilibrium must be the largest integer value of N_1 and N_2 for which the electrochemical potentials of both dots are less than zero. Otherwise, charges would escape the dots to the leads [28]. This constraint creates the characteristic honeycomb structure depicted in figure 2.14 B. For $C_M=0$, the quantum dots are independent (uncoupled), thus the gate lead coupled to one of the dots can change the number of charges inside it without affecting the number of charges on the other dot. This situation is depicted in figure 2.14 A. In figure 2.15, the electrochemical potentials around a specific set of triple-points in the linear regime are shown. The coupling degree is the same as in figure 2.14 B. The level diagrams indicate the configuration of the electrochemical potentials inside each dot. Since the linear regime is considered here, the electrochemical potentials of the source and the drain remain constant at zero and aligned with each other at all times. It is important to notice that the transport through a double quantum dot system requires the alignment of four electrochemical potential levels instead of three that it was the case in a single dot. This makes the charge transport possible only at specific points, the triple points, where the electrochemical potential levels of the two dots are aligned with those of the source and the drain. In all other electrochemical potential configurations, the system is in Coulomb blockade.

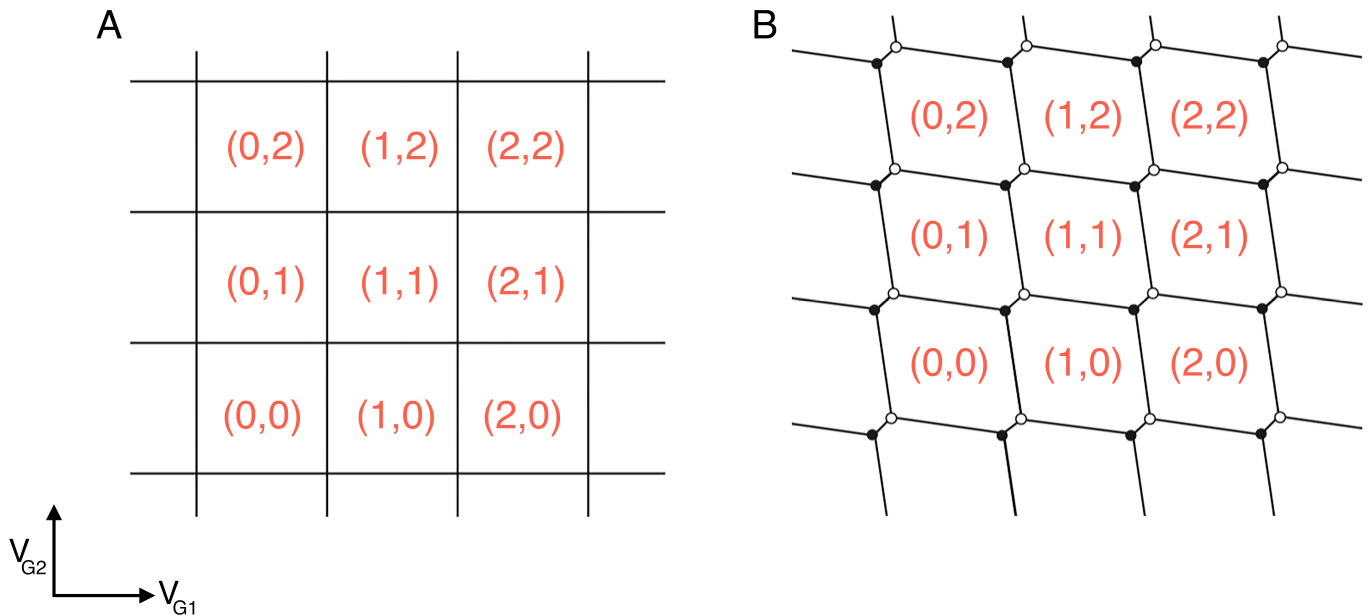


Figure 2.14: Stability diagrams for double quantum dot systems. Inside each domain the charge is constant, while on the edges of the border lines between the domains, charges can flow. The lines indicate the gate voltage values at which the number of charges changes. The number of charges on each domain is denoted by (N_1, N_2) . These diagrams can be viewed as an extension in two dimensions of the coulomb peak diagram presented in figure 2.8. In A, the capacitive coupling between the two dots is negligible, making the two dots effectively independent. In B, the inter-dot coupling capacitance is finite, resulting in a dependence between the charges on the two dots and hence, this characteristic hexagonal (or “honeycomb”) lattice is obtained. The apex of each square domain in the uncoupled dot case has now been transformed into a triple-point. Each triple-point corresponds to the edge merging of three individual honeycombs. Charge transport through the dots is possible only at these triple-points. Two types of triple-points can be distinguished, the hollow dot that corresponds to a hole transport and the solid dot that corresponds to an electron transport. The distance between the triple-points is defined by the capacitance value of the coupling between the dots (C_M). The region between the lower four domains shown in B is depicted in more detail in figure 2.15. Figure adapted from [28].

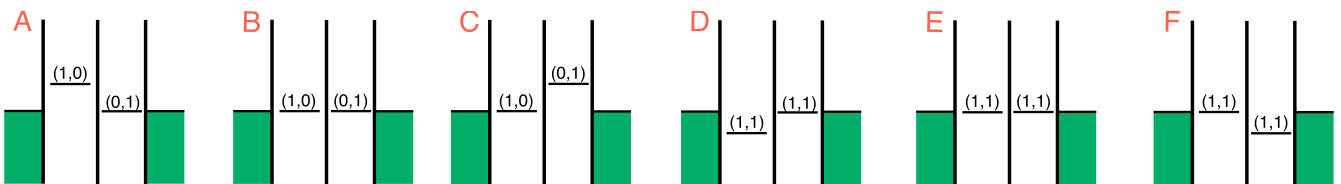
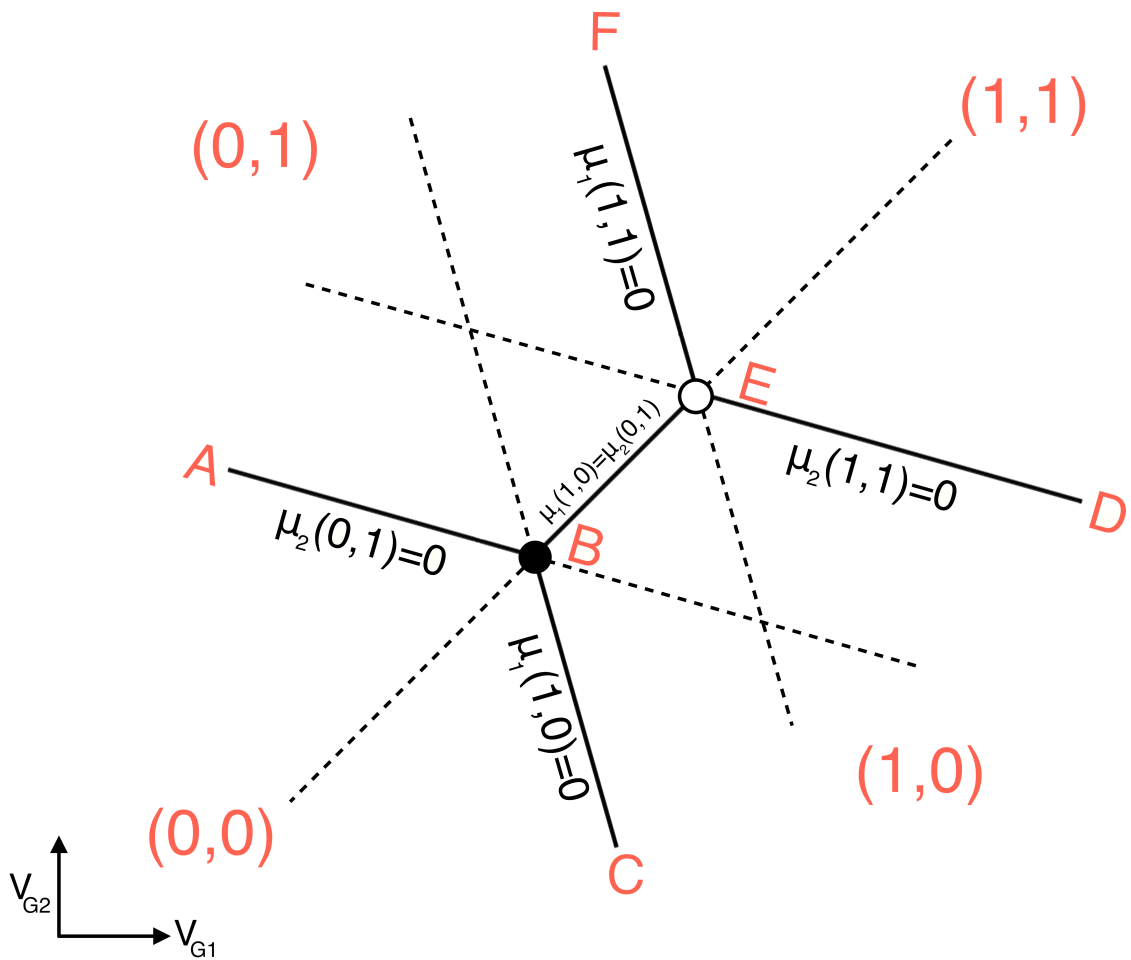


Figure 2.15: The unit cell of the honeycomb lattice of the stability diagram shown in figure 2.14 B. Four different charge domains are depicted, separated by solid lines. Each solid line indicates an alignment of an electrochemical potential level inside the dot with the electrochemical potential of either the source or the drain (both of which are set to zero volt). Solid lines marked with μ_1 and μ_2 correspond to the electrochemical potential of the first and second dot, respectively. The solid line between the triple-points designates two degenerate energy states. Each level diagram represents a configuration of the electrochemical potentials on the dot. Only in level diagrams B and E all the electrochemical potentials are aligned and thus a transport of a hole and an electron takes place, respectively. Figure adapted from [28].

Finally, the non-linear transport regime in the double quantum dot system will be considered. Now, the source-drain voltage is non-zero and hence the bias window is widened. Similar to the high-bias regime discussed in section 2.9, excited-state levels can also participate in the charge transport. Equations (2.27) and (2.28) now have a finite orbital energy term, which results in a description of the quantum transport regime. In single quantum dots, after applying a bias, the description of the system moved from coulomb peaks to coulomb diamonds. In the case of double quantum dots, the triple-points evolve to bias triangles (figure 2.16). Inside a bias triangle charge transport is allowed. The characteristic triangular shape is due to the fact that the electrochemical potential lines $\mu_1(1,0)$ and $\mu_1(1,1)$ are now equal to the potential energy difference between the source and the drain and thus, they are “pushed out” along the degenerate energy line that connects the two triple-points. The darker regions inside the triangle correspond to a transport through an excited state and they are analogue to the diagonal lines emanating from the coulomb diamonds in figure 2.11. Each base of a darker triangle, inside the main bias triangle, that runs parallel to two charge domains relates to a transport through the corresponding excited states. The rest of the unit cell features remain unchanged. The direction the triangles are pointing corresponds to the direction the current is flowing between the two dots. For a negative bias voltage, electrons move through the dot in the opposite direction and thus, the triangles in figure 2.16 will be mirrored along the degenerate energy line, signifying the flow of a current on the reverse direction.

Until now, only tunneling events between aligned energy levels were considered. This is the case where the initial and final energy states of the tunneling events have the same energy. This event is termed elastic tunneling. However, in the case of transport in the non-linear regime, tunneling also occurs when there is an energy mismatch between the initial and final states and thus, the energy levels are misaligned. This process is called inelastic tunneling. Due to the energy conservation principle, the energy mismatch between the two levels in the case of inelastic tunneling is compensated by energy exchange with the environment. Often, this translates to an absorption or emission of a photon or a phonon. A schematic representation of the differences between elastic and inelastic tunneling is given in figure 2.17. The inelastic tunneling is a second-order process, therefore its tunneling rate is much lower than the elastic tunneling rate [10].

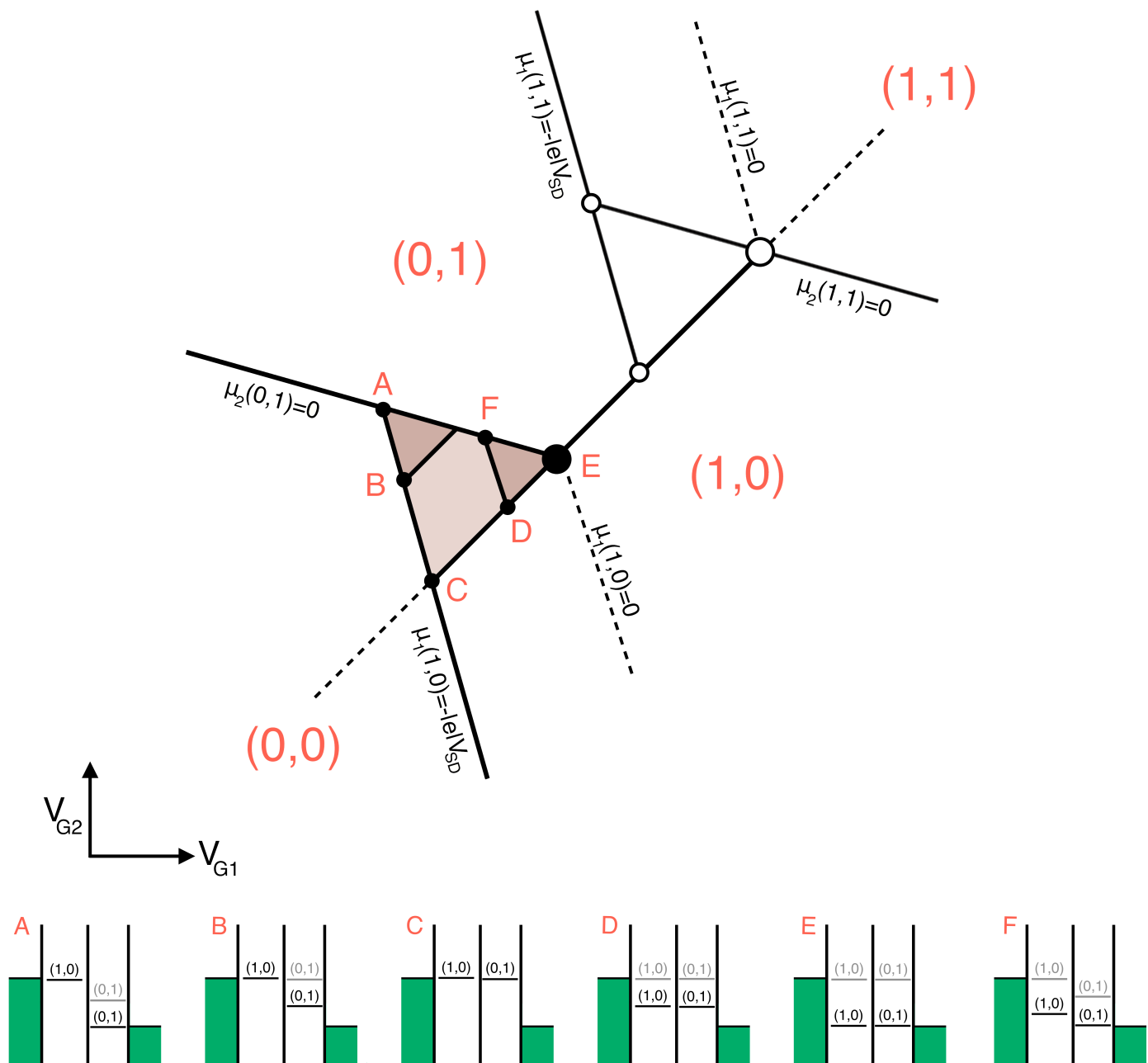


Figure 2.16: The unit cell of a honeycomb lattice for a finite bias. Energy level diagrams that correspond to the darker triangles represent a transport through an excited state. Excited states are illustrated with grey lines in the energy level diagrams. Unlike Coulomb diamonds, within this bias triangles charge transport through the dot is energetically allowed. Figure adapted from [10].

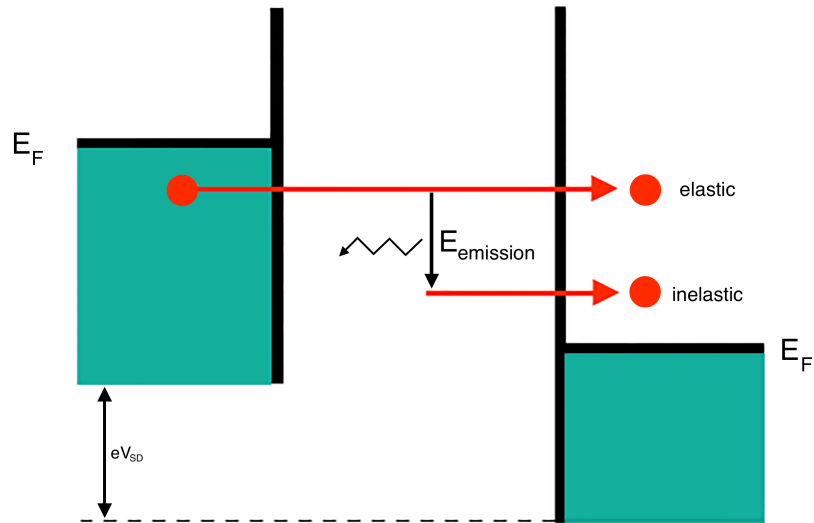


Figure 2.17: Example of the differences between elastic and inelastic tunneling. For small applied source-drain bias, the charge can tunnel through the dot from the occupied state of one reservoir to the empty state of the other, without any loss of energy. This is an elastic tunneling event. For a larger bias, the final tunneling state has lower energy than the original state, resulting in energy loss to the environment (emission of either a photon or a phonon). This is because the applied bias energy is larger than the vibrational energy $E_{emission} = \hbar\omega$. This opens a new, inelastic tunneling channel through the dot [29].

3. FABRICATION & EXPERIMENTAL METHODS

3.1 Device Architecture

The transport experiments were performed on two single-charge transistor devices with similar architecture. The designs of device I and device II are depicted in figure 3.1. The main difference between the two devices is the proximity of their plunger gates to the source-drain channel. For device II, the bottom end of each plunger is patterned closer to the bottom end of the barriers. This is expected to allow better control over the formed quantum dots. A second difference between the two devices is the configuration of their lead gates. The lead gates of device I are connected to each other, while for device II are separate. The behavior of each gate as described below is the same for both architectures.

The devices adopt a unipolar structure where two separate regions for either electron or hole transport are fabricated. To electrostatically define quantum dots in the electron side, a positive potential is applied to the electron lead gates, L_1 and L_2 , which induces a two-dimensional electron gas (2DEG) at the Si/SiO₂ interface (see figure 3.3) and then by locally depleting the gas by applying a potential to the barrier gates, B_1 , B_2 , and B_3 , two quantum dots are formed between the barriers. The barrier gates by locally depleting the gas define the dot spatially and they also control the tunnel coupling between the dot and the reservoirs by forming tunnel barriers. The lead gates are orthogonal to the barrier gates, allowing us to estimate the capacitive coupling to the dots using the parallel-plate capacitor model. By using either of the plunger gates, P_1 and P_2 , the electrochemical potential levels of each dot can be varied individually, effectively controlling the electron occupancy of the dot and therefore permitting its operation as a single-electron transistor [21]. Similarly, dots can be formed on the hole side by applying a negative potential to the hole lead gates, which now creates a two-dimensional hole gas (2DHG), and the barrier gates, B_4 , B_5 , and B_6 . By now using the plunger gates, P_3 and P_4 , the electrochemical potential levels of the dots in the hole side can be varied, controlling the hole occupancy of the dot this time. By applying a potential to two adjacent barrier gates, a single quantum dot can be formed on either side of the hole or electron side of the device. Whereas by applying a potential to all three barrier gates, a lateral double quantum dot coupled in series can be defined. The potential applied to the middle barrier will define the coupling degree of the two dots. For the potential profile of the system, refer to figure 2.12. To provide carriers to the device, n and p doped source and drain regions are used as 2DEG and 2DHG reservoirs, respectively. The source-drain leads are patterned to overlap partially with all the barrier gates for device I (see figure 3.1 A), while for device II the lead gates are patterned next to the side barriers and the two plunger gates are each partially overlapping with either the first or the third barrier gate (see figure 3.1 B).

An overview of the physics of a quantum dot was given in paragraph 1.3. Furthermore, as it was pointed out in paragraph 1.4, any of the single charge devices can also be used as a charge sensor for verifying the charge occupancy inside one of the dots across the charge sensor. In that case, the lead gates of the single electron device acting as charge sensor, are used as measuring probes.

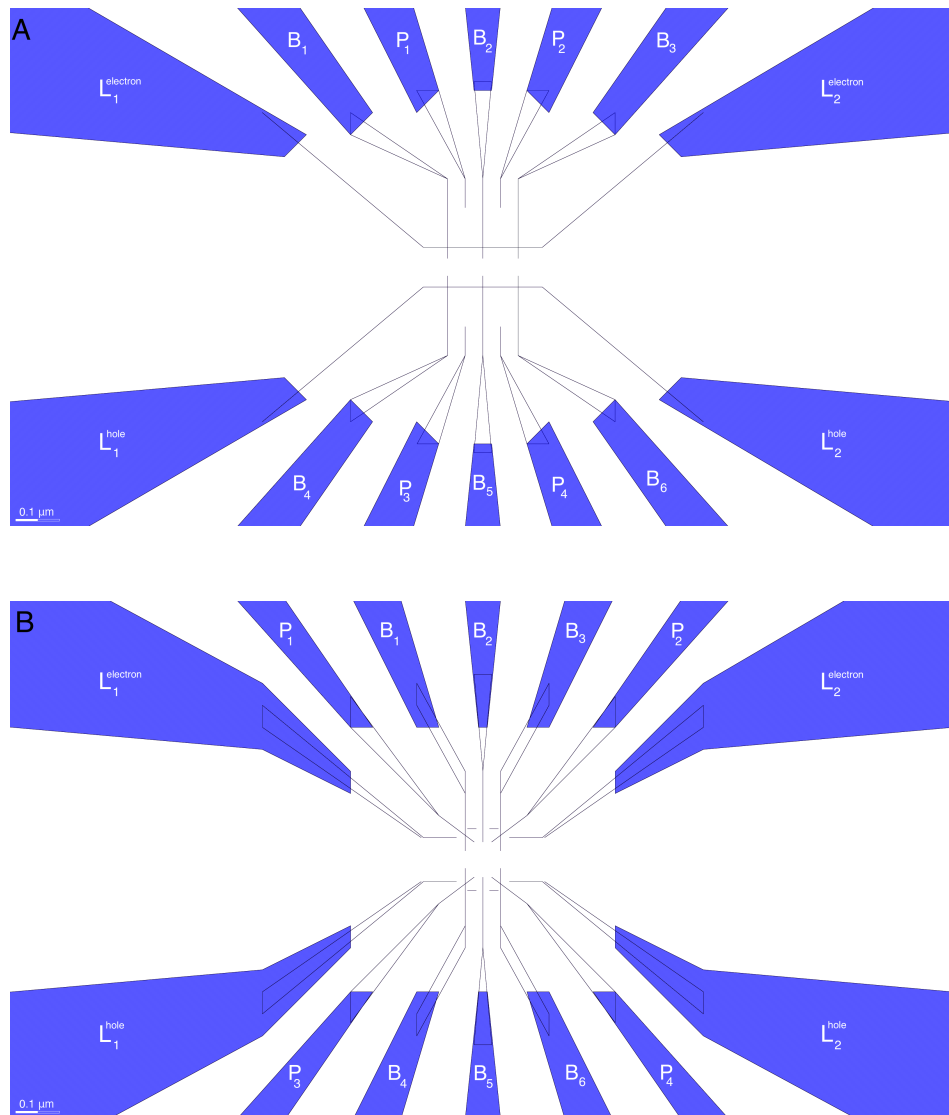


Figure 3.1: Source-drain channel design of both devices. In this area the quantum dots are formed. In 3.1 A, the channel of the device I is shown, while in 3.1 B, the channel of device II. A SEM image of the latter is given in figure 3.4. Each intentional quantum dot is formed between two of the barrier gates and underneath a plunger gate. For this area, electron beam lithography (EBL) was used for nanoscale fabrication since it is able to create structures with a size of approximately 20 nm [33]. Scale bar here is 100 nm, hence the area depicted is smaller than the wavelength of light and can not be imaged with an optical microscope.

3.2 Device Fabrication

For the fabrication of the single-charge devices, a technology similar to that used for the fabrication of integrated circuits, namely CMOS (Complementary metal–oxide–semiconductor) technology, is employed. The fabrication combines optical photolithography for wafer-scale microfabrication with electron-beam lithography (EBL) for device-scale nanofabrication. The fabrication steps are based on the recipe described by Angus et al. [30]. A near-intrinsic, high resistivity ($\rho > 10 \text{ k}\Omega\text{-cm}$ at 300 K), $\langle 100 \rangle$ oriented, silicon substrate was used for the devices. For the charge carrier reservoirs, the source and drain regions were implanted with boron (p^{++}) and phosphorous (n^{++}) dopant atoms, for the hole and electron reservoirs, respectively. For the activation of dopants, rapid thermal annealing (RTA) was used. To contact these regions, ohmic contacts were made by sputtering Ti/Pt alloy contact pads. Ohmic contacts ideally exhibit a linear current-voltage curve, thus behaving like an ideal resistor. To isolate the silicon substrate from the aluminum gate electrodes, a 10 nm thick silicon dioxide (SiO_2) layer is thermally grown at 900°C . SiO_2 is an excellent insulator, with tunneling across it becoming important only at thicknesses below 2 nm. The importance of this isolation is outlined in paragraph 2.6: the gate terminal is used merely to control the flow of charges through the source-drain channel and does not inject charges directly. Thus, the silicon dioxide layer can be thought as the isolating dielectric between two capacitor plates, with the gate forming one capacitor plate and the channel forming the other. To passivate defects at the Si/ SiO_2 interface such as dangling bonds, Al_2O_3 films were deposited on top of SiO_2 by thermal atomic layer deposition (ALD) at a substrate temperature of 250°C . There are indications that the hydrogen in the Al_2O_3 films can passivate the dangling bonds [31], which are produced when free radicals (specimens with unpaired valence electrons) exist in an immobilized environment, such as, a lattice site. Alternatively, to remove charge traps and dangling bonds, the oxide can also be annealed in pure hydrogen at 400°C and a pressure of 10 mbar [32]. After the passivation step, contact pads for the gates are defined using optical photolithography, followed by development, evaporation of Ti/Pt, and subsequent lift-off [32]. To define the aluminum barrier gate electrodes, EBL was employed. The gates were then oxidized by heating the sample for 10 minutes at a hotplate with a temperature of 160°C , effectively utilizing the aluminum oxide layer created at their surface as a dielectric. Finally, a second EBL step was performed to fabricate lead gates above all the barrier gates on device I. For device II, a second EBL step was performed to pattern plunger gates above the two side barriers and a third EBL step to pattern the second barrier and the lead gates (see the cross-sections in figure 3.5).

An image of the design of device II is shown in figure 3.2 for two different degrees of magnification. For device I this design is identical with the only difference being the order of the barrier and the plunger gate electrodes (side barrier and plunger gate electrodes on both sides are interchanged, refer to figure 3.1). On figures 3.3 and 3.4, images of the actual device are shown for two different degrees of magnification.

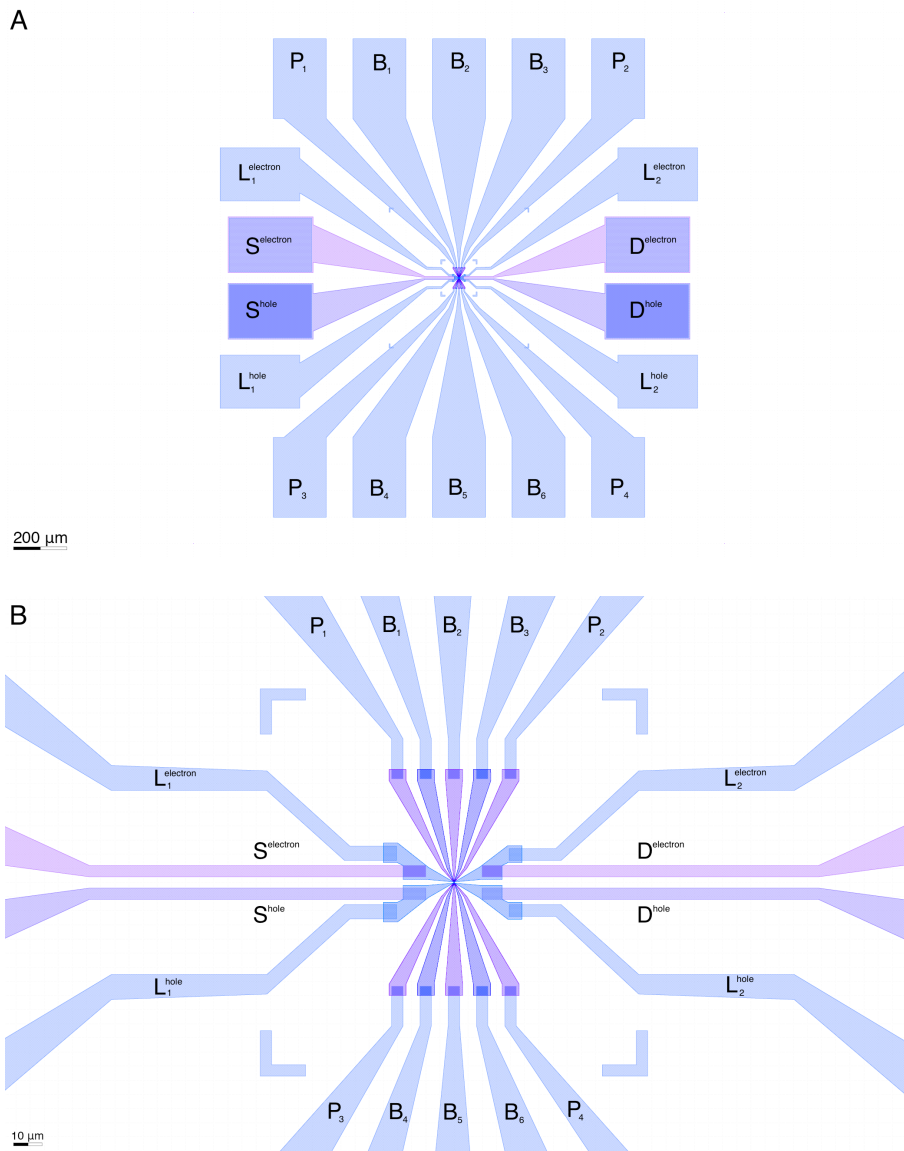


Figure 3.2: Design of device II for two degrees of magnification. In A, the device at its whole is shown. Scale bar is 200 μm and this area is visible to the naked eye. A microscopic image of the area depicted in this design is given in figure 3.3. In B, the design area in the center of the device is shown. The four markers between the vertical and the horizontal electrodes are used for alignment during photolithography for microfabrication. In A, the contact pads and part of the gate electrodes are visible. In B the gate electrodes together with the doped regions can be seen. Device I has an identical design but with interchanged side barrier and plunger gate electrodes.

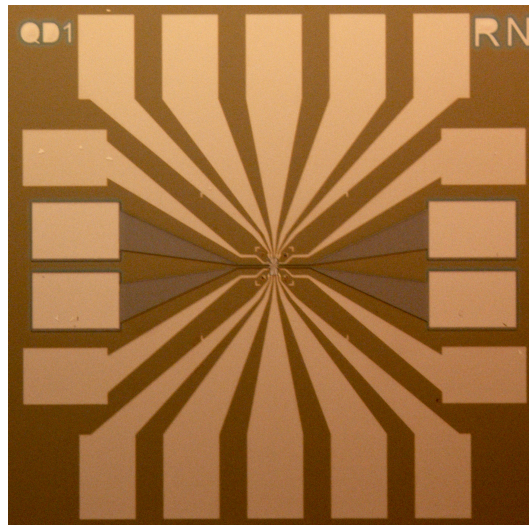


Figure 3.3: Microscopic image of device II. This device is part of a larger chip that consists of 25 similar devices. Each device on the chip has a unique two-letter identifier (top right corner).

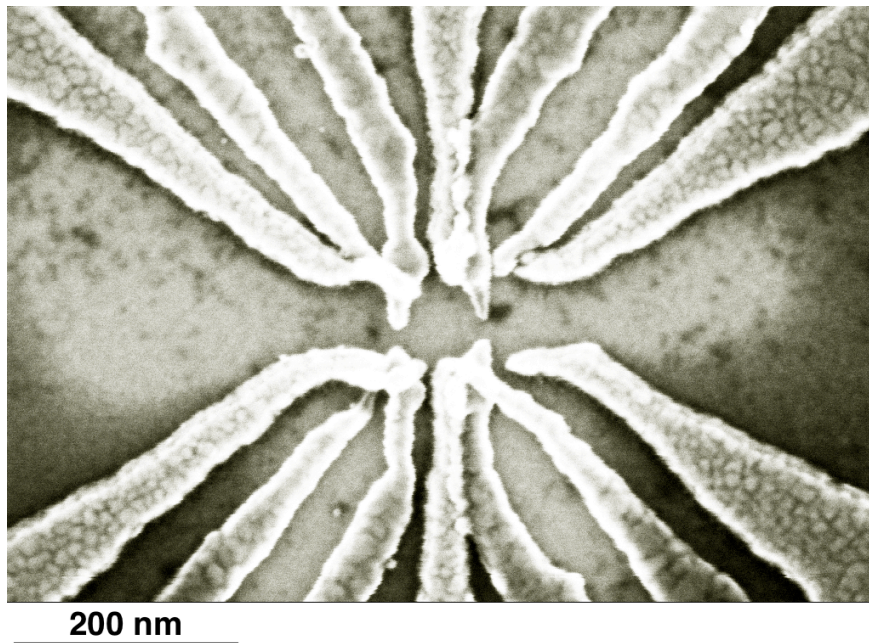


Figure 3.4: Scanning electron microscope (SEM) image of device II. The architecture of this device is shown in figure 3.1B. Images of more identical devices can be found in appendix A.

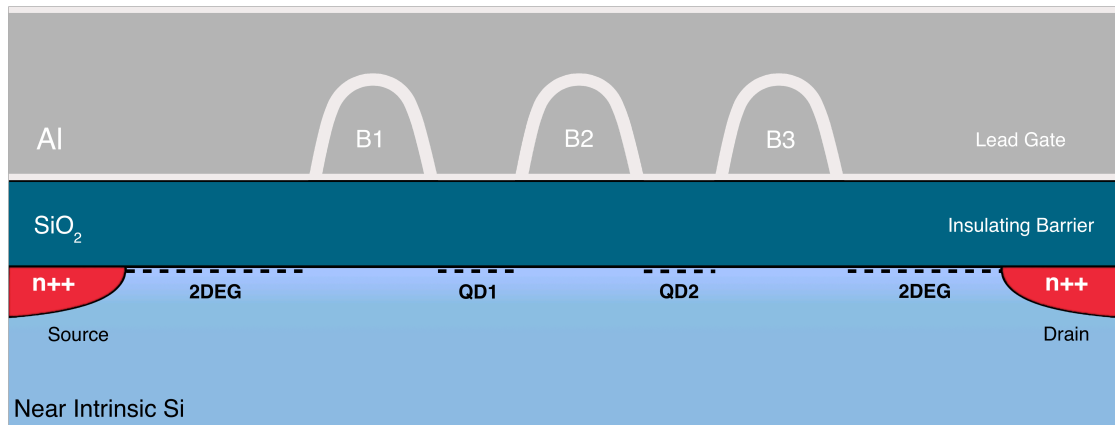
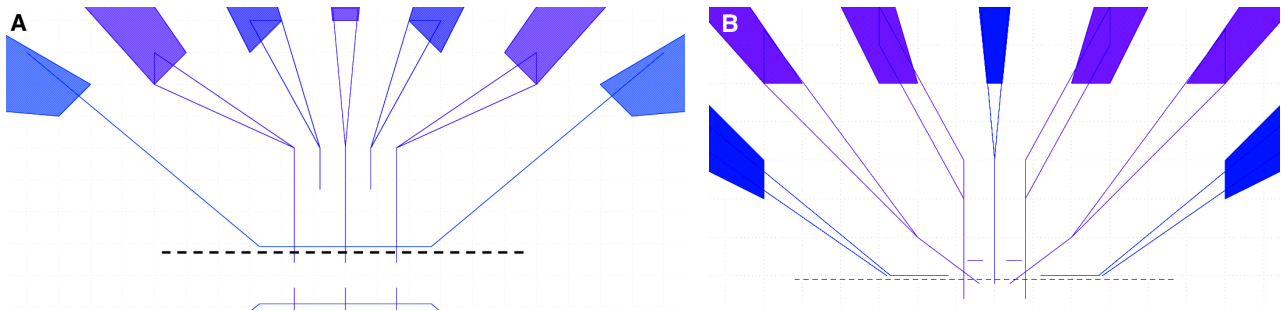
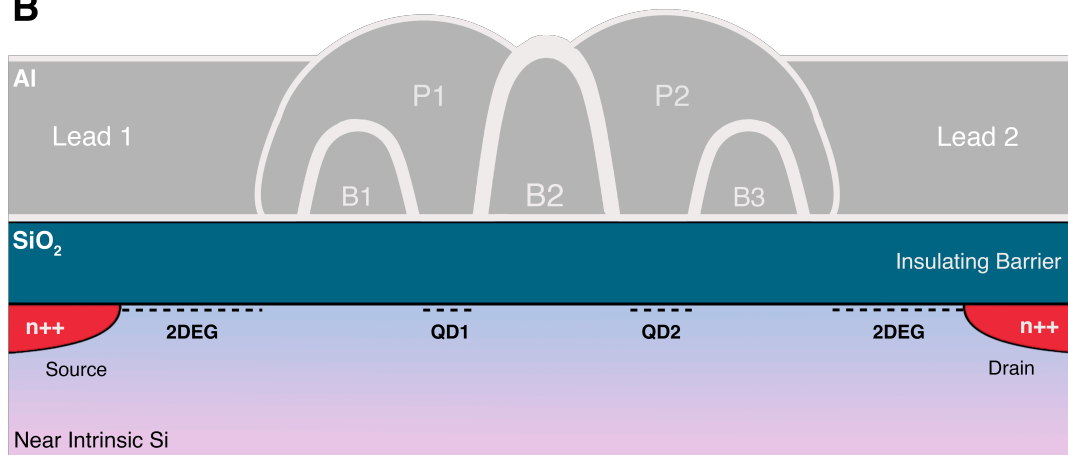
A**B**

Figure 3.5: Schematic cross-section of the electron region of devices I and II (figure 3.5 A and 3.5 B, respectively). The dashed lines in the inset figures indicate the corresponding areas of figure 3.1 where each cross-section is taken from. The lead gates, L_1 and L_2 , embedded in Al, locally deplete the electron gas, creating small carrier islands isolated from the two-dimensional electron gas (2DEG) reservoirs. These islands are the quantum dots. The barrier gates B_1 , B_2 , and B_3 control the tunnel coupling between each of the dots and the carrier reservoirs. Finally, the plunger gates, P_1 and P_2 , control the electron occupancy in each of the dots independently. Also shown, the thin layer of Al_2O_3 on top of the SiO_2 and Al layers. The hole operation region of each device is identical, but with p++ doped source and drain regions.

3.3 Measurement Setups

As discussed in paragraph 2.5, all single-charge devices are being operated at cryogenic temperatures. To achieve that, the chip that contains the single-charge devices (each chip usually consists of 25 devices in five rows of five devices each) is glued on a sample holder. The sample holder is a PCB (figure 3.6) with connection leads compatible to that of the measurement equipment used. The chip is glued onto the PCB using a synthetic polymer thermoplastic, namely Polymethyl methacrylate (PMMA), and then the PCB is heated to 80°C to evaporate solvents. A wire bonder is then used to connect the chip to the PCB contacts via aluminum wires.

Two low temperature setups were used for the characterization of the devices: a liquid helium dewar, that is accessed by a dipstick where the PCB with the chip is mounted, and a dilution refrigerator (Oxford Instruments Triton 200). The helium dewar has a base temperature of 4.2 K, while the dilution refrigerator can achieve a base temperature of less than 10 mK. Because the helium dewar allows fast loading and unloading of the chips, it is used for testing the operation of the devices, while the dilution refrigerator is used for sensitive electronic transport measurements since it is shielded and has multiple filters that can reduce the external electrical noise.

Before exposing the devices to cryogenic temperatures, a bias voltage is applied to the source and the drain leads to test whether a current flows through the source-drain channel. After submerging the device into liquid helium, a leakage test is performed. This is done by connecting a source measure unit (SMU) to one gate of the device at a time. The gate is then ramped to a positive and then to a negative voltage, while all other connections on the device are kept grounded. The SMU applies a voltage to the connected gate and at the same time measures the current to the ground. To protect the devices from overpower, the compliance is set to 0.8 nA, thus, ensuring that the current will not exceed this value while the gate voltage is ramped. A gate on the device is considered to be leaking if the current to the ground exceeds a specific value [33]. This measurement is repeated for all the gates of the device. If no leakages are detected, the turn-on characteristics of the device are then measured. To do so, a bias voltage of 10 mV is applied between the source and the drain contacts and a single voltage is applied to all the lead and barrier gates. This voltage is then ramped to positive values for the electron side and negative values for the hole side until the device is “turned-on”, this is, electrons or holes are flowing from the source to the drain. To determine the exact voltage that needs to be applied to the gates to start conducting charges, the source-drain resistance is being measured. If the device turns on successfully, electronic transport measurements can be performed.

In both setups, a low-noise IVVI-DAC rack together with a matrix module is used to conduct measurements (figure 3.7). To isolate the measurement electronics against electrical noise from the grid and to eliminate ground loops, they are powered via battery cells. Both measurement setups are custom-built at Delft University. The connection leads of the PCB where the chip is attached are wired to the matrix module. By connecting different probes from the IVVI-DAC rack to the matrix module, we can control the single-charge device and perform various transport

measurements. The DACs (digital-to-analog-converters) on the IVVI-DAC rack are used to apply gate voltages to the device. To again exclude electrical noise, the DACs are optically coupled to the computer that is used to drive them. The computer sends commands to the DACs via an optical fiber. If the voltage provided by the DACs is not sufficient, a voltage source module can be attached to the IVVI-DAC rack in order to supply a source-drain bias voltage. The rack includes an IV (current-voltage) measurement unit that converts the measured source-drain current to a voltage, that is then being measured with an external digital multimeter [33]. The data from the voltage measurements are fed to a computer and plotted using custom-built software.

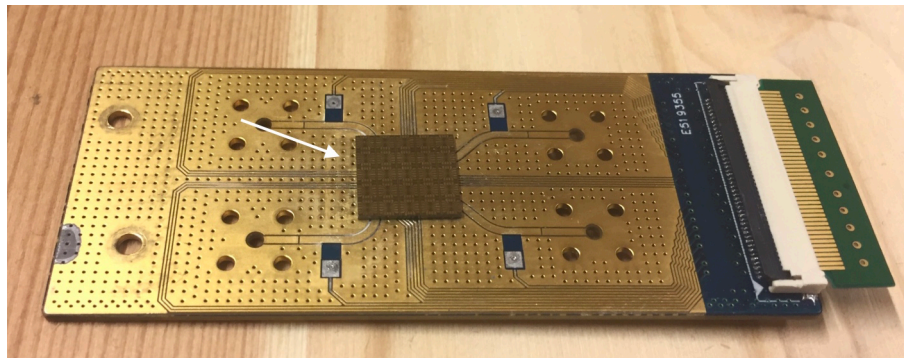


Figure 3.6: Sample holder PCB. The arrow indicates the sample (chip that contains the single-charge devices). On the right-hand side of the PCB, the female connector that attaches the PCB to the dipstick or the sample loading mechanism of the dilution refrigerator is visible. Plugged to it, a grounding PCB to avoid static discharge.

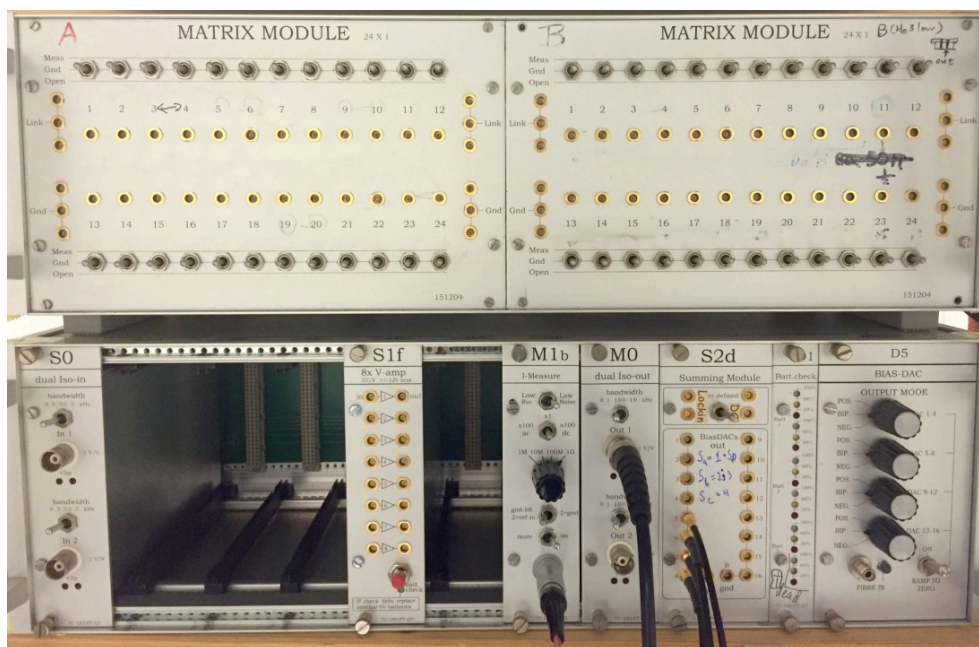


Figure 3.7: Measurement electronics. Top: two matrix modules. Each wire connected to the PCB corresponds to a connector on the matrix module. Bottom: the IVVI-DAC rack. From the left: the third module on the IVVI-DAC rack is the IV measurement unit and the fifth module contains the digital-to-analogue converters discussed in the text.

4. RESULTS & DISCUSSION

4.1 Electron Transport on Device I

First, the turn-on characteristic of the electron operation region of device I is investigated. The same voltage V_G is applied to all barrier, plunger, and lead gates on the electron operation region, while the gates of the hole region are kept grounded. At the same time, a constant bias voltage $V_{SD} = 1$ mV is applied to the source-drain channel. The gate voltage V_G is then ramped to positive values while the resulting channel current, I_{SD} , is being measured. Once a threshold voltage V_{TH} has been reached, the conduction band has been pulled below the Fermi energy level and energy states on the dot are available for occupation (recall the first potential profile in figure 2.5). This signifies the onset of a flow of electrons from the source to the drain reservoirs and subsequently the flow of a tunneling current. As soon as this flow starts the device is considered to be “turned-on”. This turn-on behavior is depicted in figure 4.1. The threshold voltage V_{TH} has been measured to be approximately 2.6 V while the source-drain current reaches a value of roughly 7.3 nA.



Figure 4.1: Turn-on characteristic curve measured at $T \approx 4.2$ K and for a bias voltage $V_{SD} = 1$ mV. A gate voltage V_G is applied simultaneously to all gates on the electron operation region, while the hole operation region is kept at zero voltage.

Next, the ability of the barrier gates to tune the conduction of electrons in the source-drain channel below the barriers is assessed. By ramping the barrier gate voltage of each individual barrier to a lower value while simultaneously keeping the voltage of all the other gates to a value above the threshold voltage determined previously, the “pinch-off” curve of each barrier has been obtained (figure 4.2). The “pinch-off” curve determines the ability of the barrier gate voltage to tune each individual potential barrier from highly transparent to opaque, which corresponds to a high and a negligible current flow, respectively. This is equivalent to saying that the barrier gate pinches-off the tunnel coupling between the quantum dot and the carrier reservoirs, effectively controlling the tunnel rate across the barrier (recall the discussion in chapter 2.1). From the “pinch-off” curves in figure 4.2, we can conclude that each barrier can individually control the conduction channel for different barrier gate voltages. Additionally, we observe some minor resonances in

the measured current that can be attributed to random conductance fluctuations due to trap states or thermal noise. Fluctuations due to thermal noise usually change with every sweep.

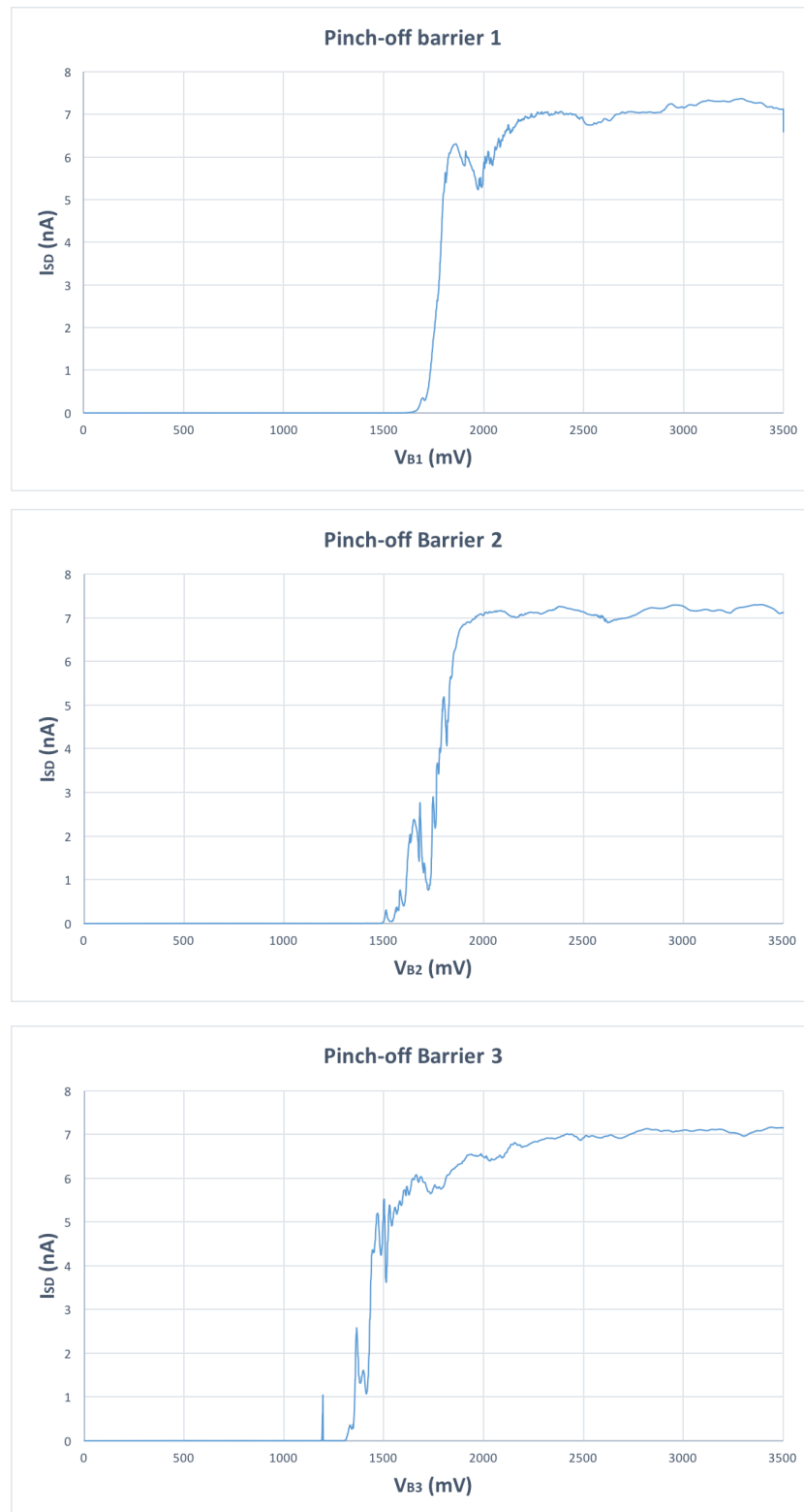


Figure 4.2: Pinch-off characteristic curves measured at $T \approx 4.2$ K and for $V_{SD} = 1$ mV. A gate voltage of 3.5 V is applied simultaneously to all gates on the electron operation region except the pinch-off barrier. The hole region is kept at zero voltage.

Subsequently, we measure the source-drain current as a function of the applied barrier voltages of B_1 and B_2 , while keeping the bias voltage V_{SD} constant at 1 mV, and the voltage of the unused barrier B_3 and the lead voltage, V_L , constant at 3.5 volts. The gates at the hole operation region are kept grounded. The range the barrier voltages of B_2 and B_3 were ramped at, was chosen to be near the pinch-off range of each barrier as determined from the previous measurement. Recall from section 2.7 that each charge transition through a quantum dot appears as a peak in the conductance versus gate voltage plot. This Coulomb peak will appear as a parallel diagonal when two barrier gates are swept versus each other. The source drain current is usually represented in a two-dimensional plot as a variation in the color of each transition diagonal. The nature of these lines can be understood as follows: the gates defining the tunnel barriers are also coupled to the quantum dot capacitively [34]. Every time the voltage of the barrier gate is changed, the tunnel coupling is changed resulting to a change in the current flow (represented with the color variation) and at the same time, due to the capacitive coupling, the electrochemical potential on the dot is altered (recall equation 2.18). As discussed in chapter 2, this change shifts the “ladder” of electrochemical potential levels on the dot up or down, allowing new potential levels to be aligned within the bias window, which results on new parallel diagonals. The slope of this diagonal is a measure of the capacitive coupling ratio of the dot to the two barrier gates.

This series of parallel charge transition diagonals is observable in the measurement shown in figure 4.3. The large number of periodic oscillations is an indication that the dot is not due to defects, but intentional. The capacitive coupling ratio is found from the barrier versus barrier scan to be $C_{B_2}/C_{B_1} \approx 0.95$, indicating the existence of a quantum dot strongly coupled between the two barriers. The assumed location of the dot can be approximated from the capacitive coupling ratio and it is depicted in figure 4.4. The measured source-drain current as a function of the voltage applied to B_2 (figure 4.5) exhibits the characteristic Coulomb oscillations in the many-electron regime. Recall from the discussion in section 2.7 that each peak in the current corresponds to a change in the charge occupancy of the dot, while each valley between the peaks corresponds to a Coulomb blockade situation. The irregularities on the spacing between the Coulomb peaks is due to the dependence of the addition energy to a non-constant orbital energy term (recall equation 2.20). The peak heights vary with the barrier gate voltage, as expected for tunneling via single quantum states (see [27] for a discussion of this phenomenon). The ability to control the electron occupancy of the dot when sweeping the voltage of B_2 demonstrates that the device can be operated as a single-electron transistor.

Furthermore, the barrier versus barrier scan reveals two more sets of transition lines, nearly parallel to the x and y -axis, respectively. This is attributed to the formation of intentional or unintentional (formed by disorder in the oxide or the silicon-oxide interface) quantum dots between gates in close proximity to the scanned area. These dots are also capacitively coupled to either of the barriers B_1 and B_2 . Therefore, when these dots are occupied by charges, their electrostatic field influences the potential profile of the quantum dot formed between B_1 and B_2 . This effect of charge redistribution in the gate space can be utilized for charge sensing. By coupling capacitively two adjacent quantum dots on the same operation region or two

quantum dots formed on two different operation regions across each other, we have demonstrated that this device can be operated as a non-invasive charge sensor. Recall from the discussion in chapter 1 that charge sensors allow the confirmation of charge confinement inside quantum dots and the readout of their spin state.

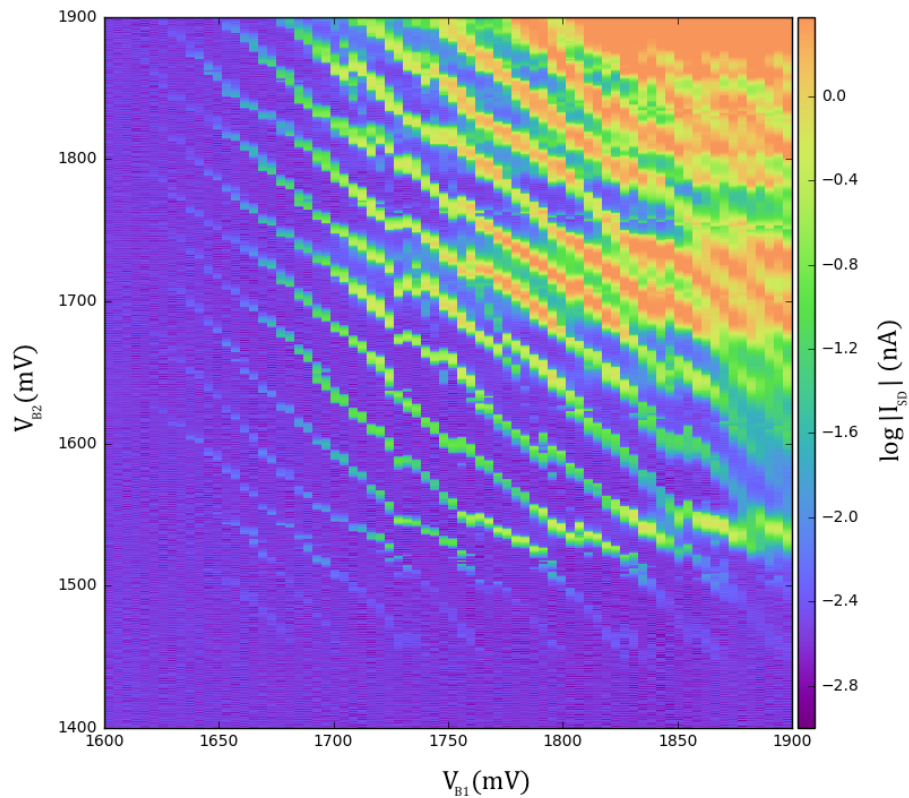


Figure 4.3: Source-drain current as a function of V_{B1} and V_{B2} measured at $T = 50$ mK for $V_{SD} = 1$ mV, $V_{B3} = 3500$ mV, and $V_L = 3500$ mV. The current is plotted in a logarithmic scale. Series of parallel charge transition diagonals and charge transition lines parallel to the two axes are visible.

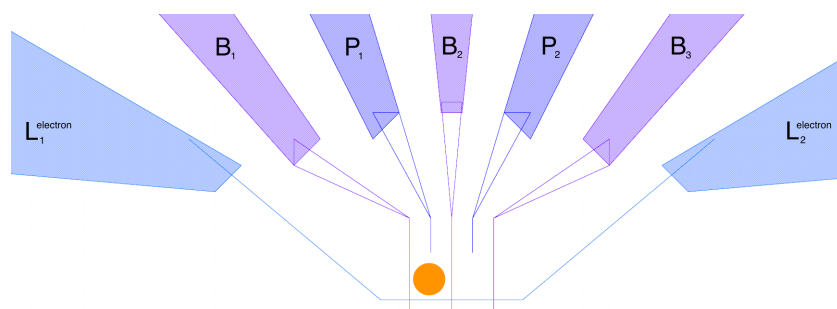


Figure 4.4: Assumed location of the quantum dot between the barriers (orange circle) extracted from the capacitive coupling ratio $C_{B2}/C_{B1} \approx 0.95$.

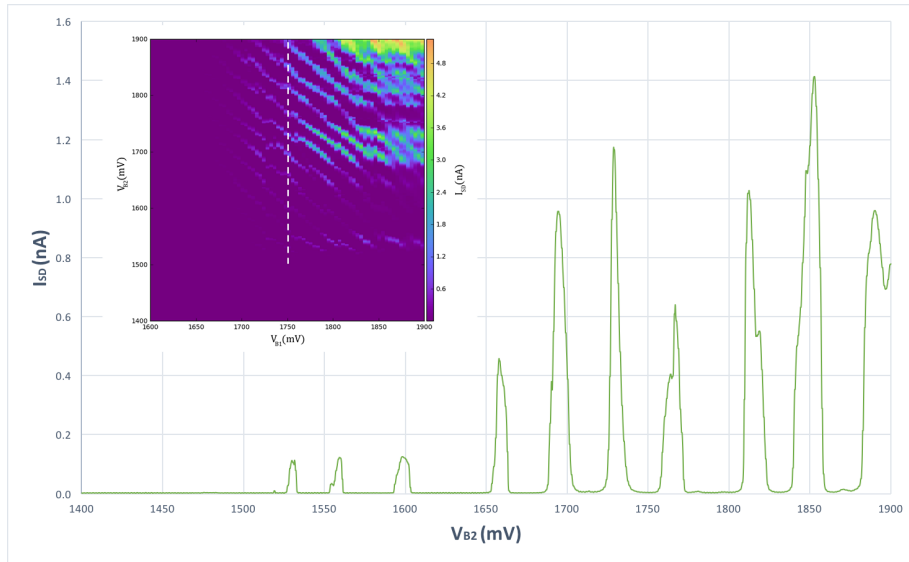


Figure 4.5: Coulomb peaks in the source-drain current measured at $T = 50$ mK for $V_{B1} = 1752$ mV, $V_{SD} = 1$ mV, $V_{B3} = 3500$ mV, and $V_L = 3500$ mV. As expected, the Coulomb peaks show different amplitudes and are irregularly spaced. Inset: the dashed line indicates the area of the barrier versus barrier scan where the Coulomb peaks were measured. Notice the linear current scale.

A second barrier versus barrier scan was performed, this time for the two side barriers, B_1 and B_3 . The voltage of B_2 was set to 1.5 V, while the the bias voltage V_{SD} was kept constant at -2 mV and the lead voltage V_L at 3.5 volts. The gates at the hole operation region were grounded. This resulted in the formation of a set of double quantum dots. As it was elaborated in section 2.10, since the the non-linear transport regime is considered here, the transport through the dot resulted in the formation of bias triangles (see figure 4.6). By mapping the bias triangles in more detail, features inside them as described in figure 2.16 could be observed.

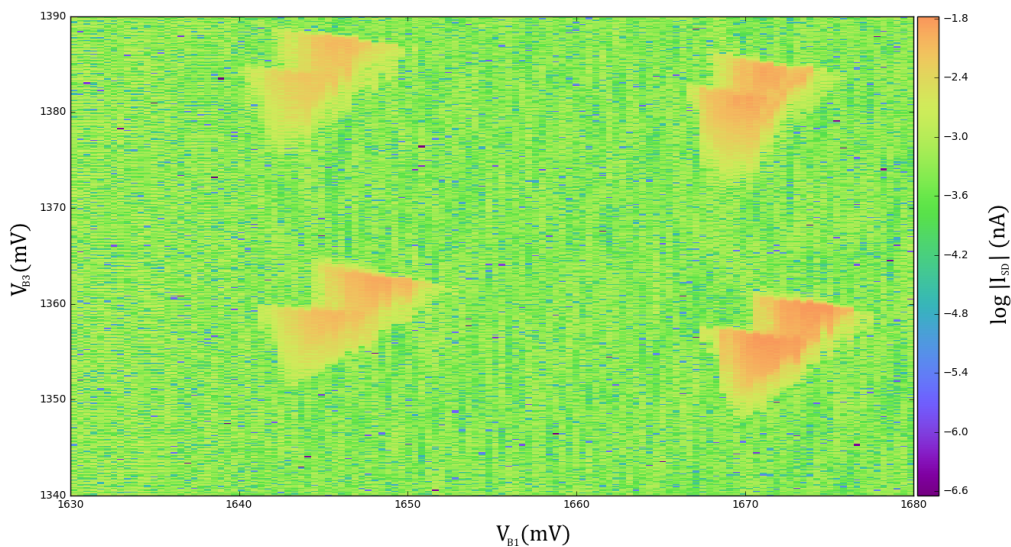


Figure 4.6: Bias triangles observed in the non-linear transport regime of the double quantum dot. Data recorded at $T = 50$ mK for zero magnetic field.

Last, a source-drain bias spectroscopy was performed. The differential conductance of the source-drain channel for different values of source drain voltage, V_{SD} , and hole operation region gate voltage, V_{HG} , is being measured (figure 4.7). Because of the proximity of the hole operation region to the electron operation region, the gates of the hole region can be utilized as a plunger gate for the electron region if their voltage is varied simultaneously. From the B_1 versus B_2 scan the voltage of the first barrier, V_{B1} , was chosen to be 1.7 V and that of the second barrier, V_{B2} , was chosen as 1.5 V. These values correspond to the last charge transition diagonals. Furthermore, the voltage of the barrier B_3 was set to 2 V and the lead voltage, V_L , to 4 V. V_{HG} was varied between -1 and -0.1 V.

The presence of well-defined Coulomb diamonds in the scan indicates the periodical change in conductance due to the Coulomb blockade effect as it was discussed in chapter 2. As the voltage of the hole operation region gates, V_{HG} , was reaching more negative values, the charging energy of the dot (height of diamonds) was increased. This is an indication that the quantum dot was shrinking in size (due to changes in its capacitance) and therefore approaching the single-electron limit. The charging energy varies approximately from 0.5 to 10 mV. For $V_{HG} < -0.5$ V the diamonds do not close completely anymore. This can be due to impeded conduction because of charge occupation of trap states or dots defined elsewhere in the gate space. However, the diamonds have well-defined periodicity, indicating that a main quantum dot is dominating the charge transport. Furthermore, clear lines of increased conductance appear emanating and running parallel to the diamond edges outside the Coulomb blockade region. Recall from the discussion in section 2.9 that these lines correspond to the presence of extra available transport channels due to excited energy states (such as orbital excited states). The precise nature of these excited states is however unknown.

It is hard to conclude whether the last electron on the dot was reached or not in this measurement. The presence of a conduction peak on the bias spectroscopy at $V_{HG} \approx -1$ V for $V_{SD} = -10$ mV indicates that at least one more electron occupied the quantum dot for $V_{HG} < -1$ V. Therefore, a second scan was performed in the same gate space area where V_{HG} was varied between -1.3 and -0.3 V (figure 4.8). This measurement indeed verifies the hypothesis that more electrons occupied the quantum dot. Although the high charging energy of the last diamond is a strong indication that the few-electron regime has been reached, it is still not possible to ascribe the opening of the last diamond at $V_{HG} \approx -1.2$ V to the last occupied electron state in the dot, since the conductance of the channel might have dropped below the thermal noise level. There are strong indications however that this device architecture can potentially reach the few-electron regime.

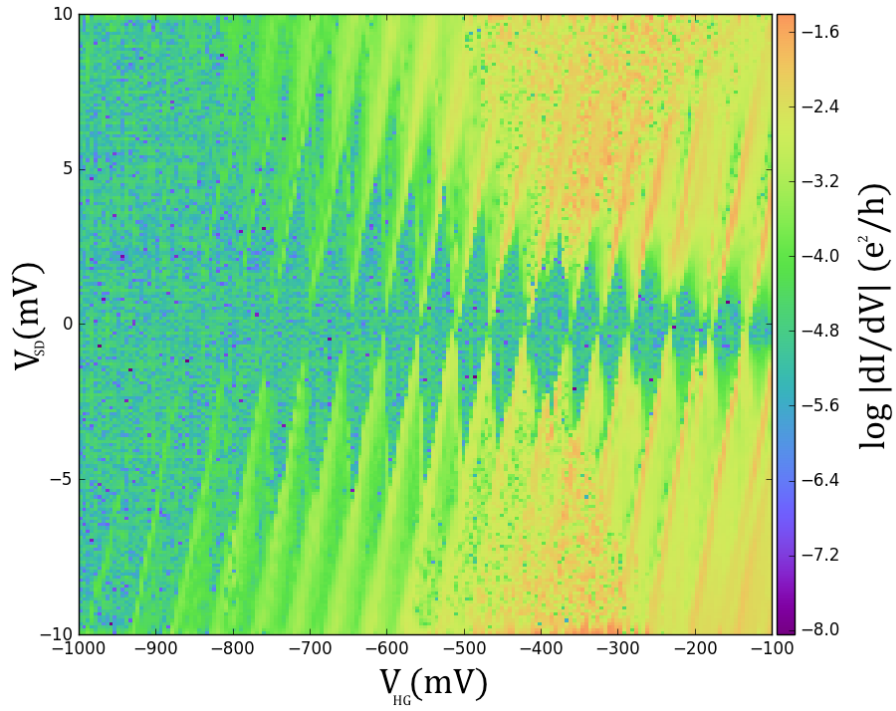


Figure 4.7: Bias spectroscopy performed at $T = 50$ mK for $V_{B1} = 1700$ mV, $V_{B2} = 1500$ mV, $V_{B3} = 2000$ mV, and $V_L = 4000$ mV. Well-resolved Coulomb diamonds and excited states manifested as high-conductance lines are observable.

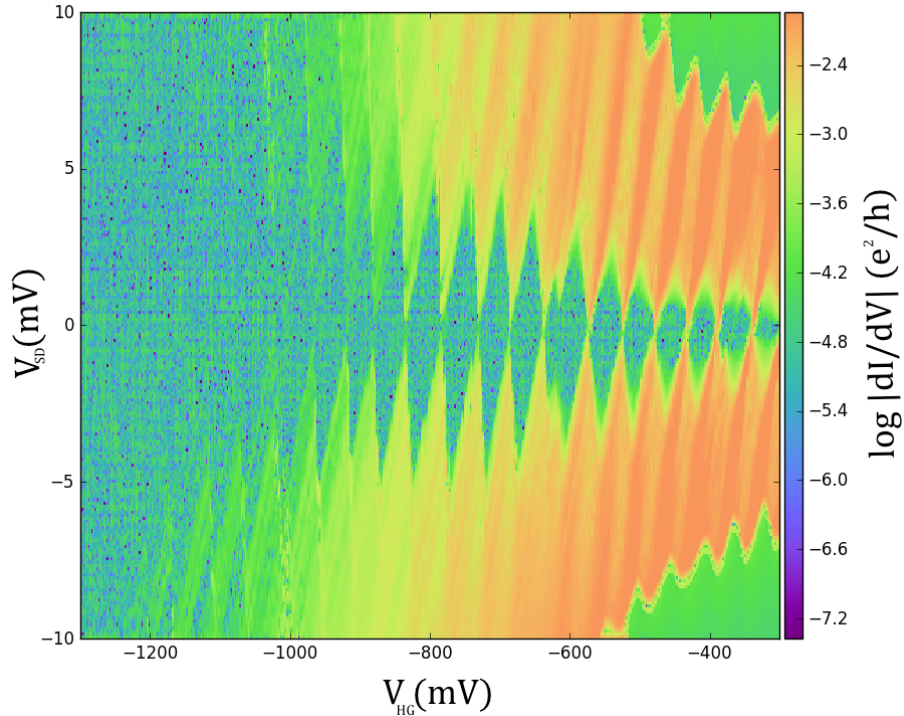


Figure 4.8: Bias spectroscopy performed at $T = 50$ mK for $V_{B1} = 1710$ mV, $V_{B2} = 1710$ mV, $V_{B3} = 2000$ mV, and $V_L = 4000$ mV. Coulomb diamonds down to the few-electron regime can be resolved.

To conclude, we have demonstrated that it is possible to control the electron transport at 4.2 K and 50 mK via the barrier and lead gates of device I, the architecture of which was presented in chapter 3. We have reported the formation of single and double intentional quantum dots, and the single-electron tunneling in the few-electron regime. Additionally, the capability of the device to operate as a charge sensor has been demonstrated. To gain better control over the formation of the quantum dots and reach the single-charge regime in the dot occupancy, a new device design was realized, that of device II as presented in chapter 3. Its electronic characterization results follow in the next section.

4.2 Electron Transport on Device II

Equivalently to the first measurement, the turn-on characteristic of the electron operation region of device II is studied. This turn-on behavior is depicted in figure 4.9. The threshold voltage V_{TH} has been measured to equal approximately 2770 mV while the source-drain current reaches a value of roughly 0.97 nA.

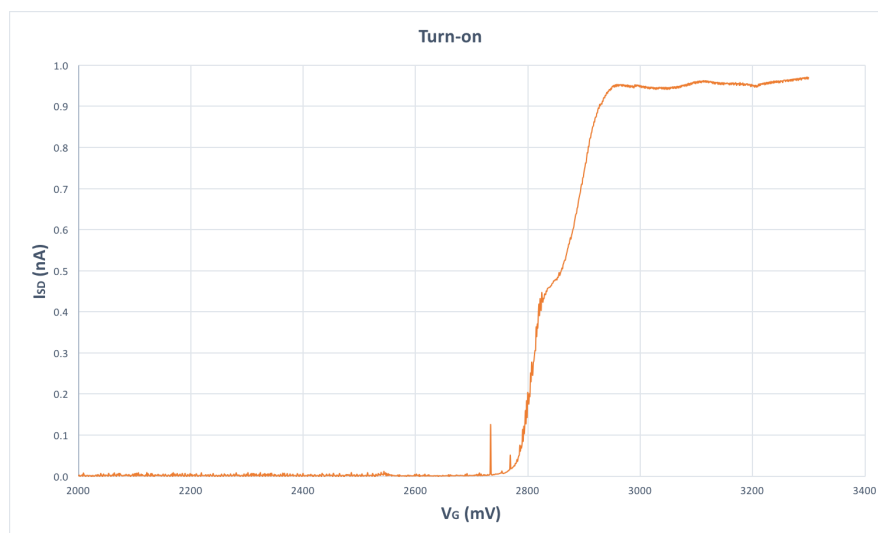


Figure 4.9: Turn-on characteristic curve measured at $T \approx 4.2$ K for a source-drain bias voltage $V_{SD} = 1$ mV. A gate voltage V_G is applied simultaneously to all gates on the electron operation region, while the hole operation region gates are grounded.

Next, the ability of the barrier gates to tune the conduction from highly transparent to opaque is assessed. This is done by measuring the “pinch-off” curve of each barrier. As it can be seen in figure 4.10, both B_1 and B_2 can individually pinch off the conduction channel of the device for different barrier gate voltages, although B_2 exhibits a somewhat lesser degree of influence over the conduction. B_3 didn’t exhibit a pinch-off characteristic, this could be an indication of some type of gate damage, such as a metal discontinuity, or even of the total absence of the gate (see images in appendix A).

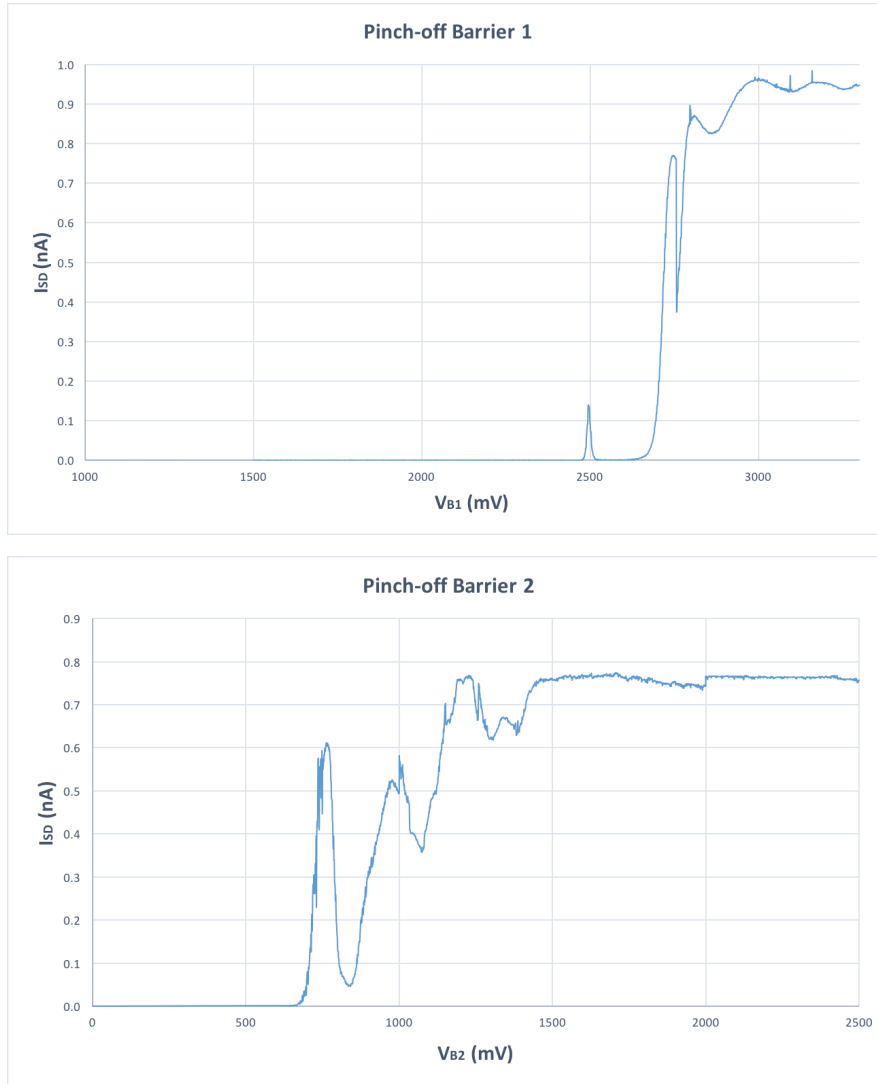


Figure 4.10: Pinch-off characteristic curves measured at $T \approx 4.2$ K for a bias voltage of $V_{SD} = 1$ mV. A gate voltage of 3 V is applied simultaneously to all gates on the electron operation region except the pinch-off barrier. The hole region is grounded.

Last, the source-drain current as a function of the applied barrier voltages of B_1 and B_2 was measured. V_{SD} was kept constant at 1 mV, and the voltage of both lead gates, V_{L1} and V_{L2} , at 3 V. The gates at the hole operation region were set to -1 V in order to act as a plunger gate (see discussion in the previous section). The result of this scan is shown in figure 4.11. The existence of a single well-defined transition line and the inability to form well-defined diamonds in the spectroscopy scan (see measurement in figure B.1 in appendix B) indicate that the dot is probably unintentional, formed because of local fluctuations on the potential due to the charge occupation of trap states in the oxide or the silicon-oxide interface. Furthermore, a constant voltage of 3 V was applied to the two plunger gates and the same area was mapped again. The resulting image of this scan exhibits the same features as in figure 4.11 (see measurement in figure B.2 in appendix B), indicating that the plunger gates have no influence over the charge occupation of the quantum dot.

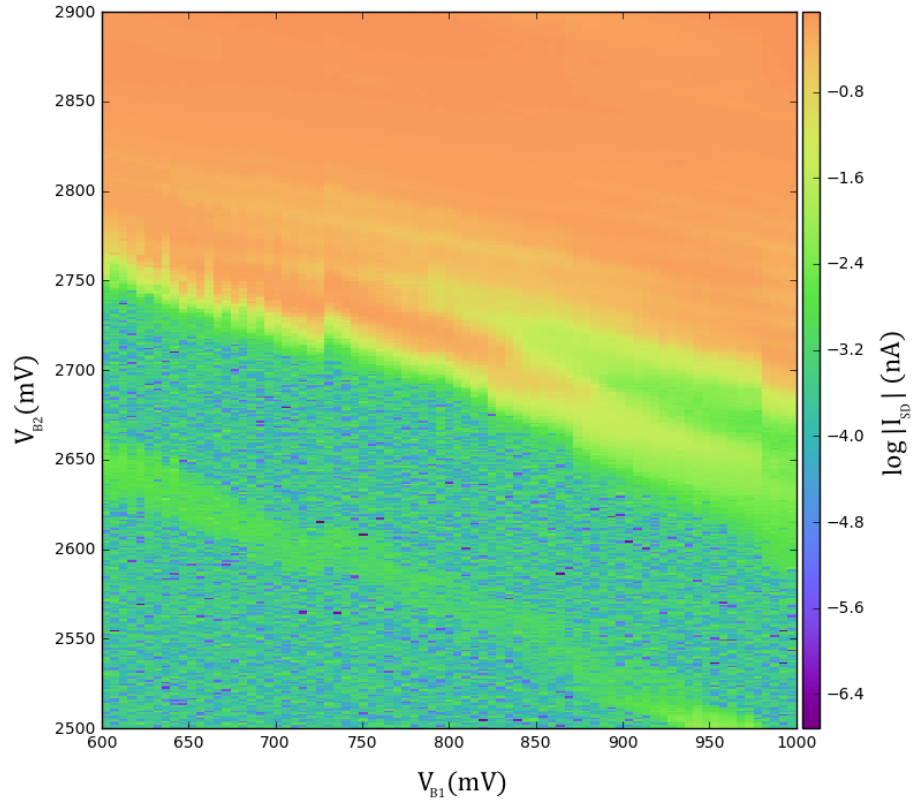


Figure 4.11: Source-drain current as a function of V_{B1} and V_{B2} measured at $T \approx 4.2$ K for $V_{SD} = 1$ mV, $V_{L1} = V_{L2} = 3500$ mV, and $V_{HG} = -1000$ mV. The current is plotted in a logarithmic scale. The existence of a single well-defined parallel charge transition diagonal indicates the existence of an unintentional quantum dot.

4.3 Hole Transport on Device II

Similarly, the turn-on characteristic of the hole operation region of device II is studied. The gate voltage, V_G , applied to all gates is now ramped to negative values, while the bias voltage, V_{SD} , remains at 1 mV. The gates in the electron region are grounded. When a threshold voltage V_{TH} has been reached, the valence band has been pulled above the Fermi energy level and hole energy states on the dot are available for occupation (recall the second potential profile in figure 2.5). Analogously to the electron transport, this signifies the onset of a flow of holes from the source to the drain reservoirs and subsequently the flow of a tunneling current. The turn-on behavior of the device is depicted in figure 4.12. The threshold voltage V_{TH} has been measured to be -730 mV while the source-drain current reaches a value of 0.9 nA.

Next, the ability of the barrier gates to tune the conduction of holes in the source-drain channel below the barriers is assessed. During the leakage test it was found the B_1 was leaking to B_3 , suggesting that the two barriers were physically connected to each other, a circumstance attributed to issues during the fabrication process. Thus, during all tests, the voltage of these two barriers was ramped simultaneously. By ramping the applied barrier gate voltage of first B_1 and B_3 , and then B_2 to a more negative value while concurrently keeping the voltage of all the other gates to a value above the threshold voltage determined previously, the “pinch-

off” curve of each barrier has been obtained. All the gates of the electron operation region were now set to a voltage of 1000 mV. A positive voltage applied to these gates would effectively utilize them as a plunger gate, as it was demonstrated during the prior transport experiments. As it can be seen in figure 4.13, B_1 and B_3 can pinch off the conduction of the channel when we apply a voltage to them simultaneously. B_2 also exhibits an influence over the conduction of the channel, but to a lesser extent (figure 4.14). This can be attributed to a displacement of the gate during fabrication.

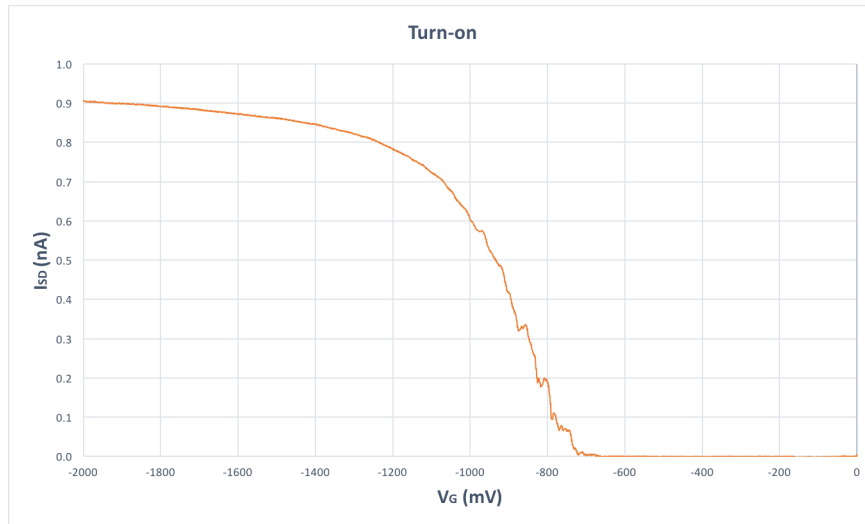


Figure 4.12: Turn-on characteristic curve measured at $T \approx 4.2$ K for $V_{SD} = 1$ mV. A negative voltage V_G is applied simultaneously to all gates on the hole operation region, while the gates of the electron operation region are kept grounded.

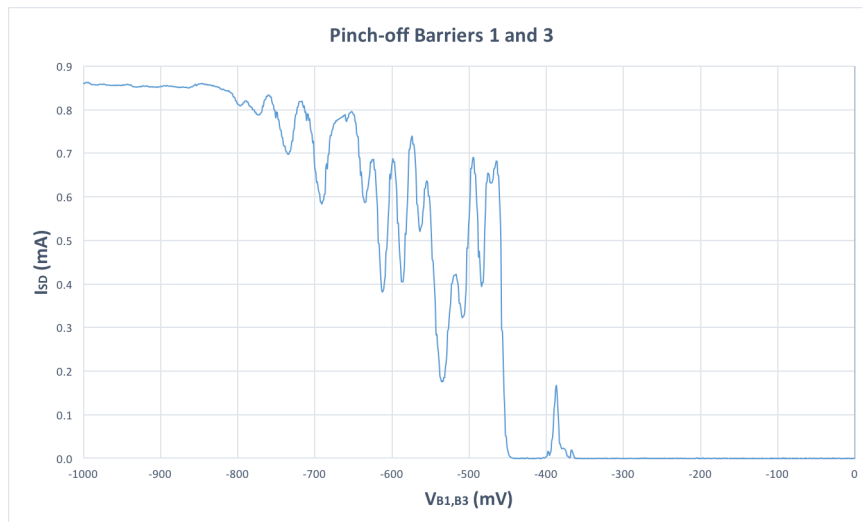


Figure 4.13: Pinch-off characteristic curve of both B_1 and B_3 measured at $T \approx 4.2$ K for a bias voltage of $V_{SD} = 1$ mV. Resonances in the measured current due to conductance fluctuations can be observed.



Figure 4.14: Pinch-off characteristic curve of B_2 measured at $T \approx 4.2$ K for a bias voltage of $V_{SD} = 1$ mV.

Finally, the source-drain current as a function of the applied barrier voltages of B_1 and B_3 , and B_2 was measured for two different voltage values of the gates of the electron operation region operating as a plunger gate, $V_{EG} = 1200$ mV and $V_{EG} = 2000$ mV, respectively. The source-drain current was also measured as function of the same applied barrier voltages of B_1 and B_3 , and V_{EG} , while V_{B2} was kept at zero voltage. The results are summarized in figures 4.15 and 4.16. Transition lines attributed to a transfer via an intentional quantum dot can be distinguished on all scans. The somewhat large number of periodic oscillations is an indication that the dot is not due to trap states. From the slope of these lines can be deduced that the dot demonstrates a strong capacitive coupling to B_1 and B_3 , and to the electron operation region gates and a weak coupling to B_2 , something expected from the pinch-off characteristic curve of this barrier. However, it is not possible to determine the exact position of the dot in the gate space, since it can not be concluded whether it is B_1 or B_3 that pinches off the channel at a particular voltage. Another scan, this time between B_1 and B_3 , and the plunger gates of the hole operation region was performed (measurement can be found in figure B.3 in appendix B). The parallel to x-axis lines indicate coupling solely to the barrier gates. Hence, it has been demonstrated again that the plunger gates have no influence over the charge occupation of the quantum dot in this particular device.

Figure 4.17 depicts the measured source-drain current as a function of the voltage applied to B_2 and B_3 . The current exhibits the characteristic Coulomb oscillations in the many-hole regime. The ability to control the hole occupancy of the dot when sweeping the voltage of the barriers is an indication that the device can be operated as a single-charge transistor.

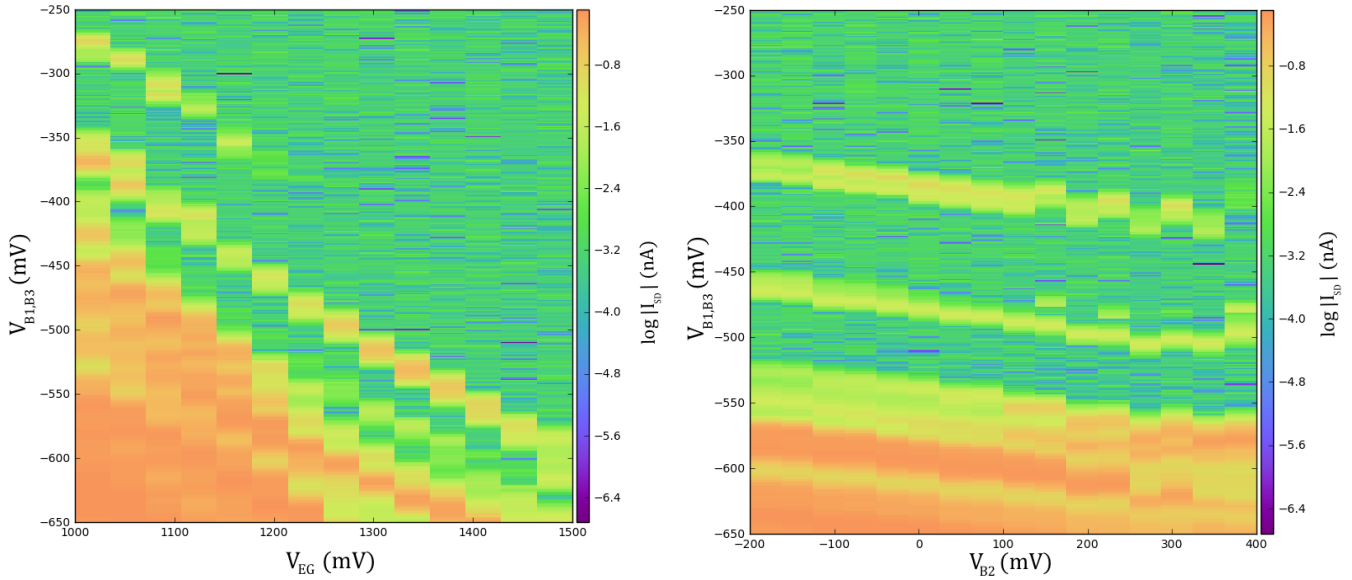


Figure 4.15: Source-drain current as a function of V_{B1} and V_{B3} , and the voltage applied to the gates at the electron operation region (left) or V_{B2} (right). Both measured at $T \approx 4.2$ K for $V_{SD} = 1$ mV and $V_{L1} = V_{L2} = -2000$ mV. For the scan on the left $V_{B2} = 0$, while for the scan on the right $V_{EG} = 1200$ mV. The current is plotted in a logarithmic scale. The abrupt termination of the first transition line on the scan on the left can be an indication of an unintentional quantum dot, the influence of which was eliminated after applying a larger V_{EG} .

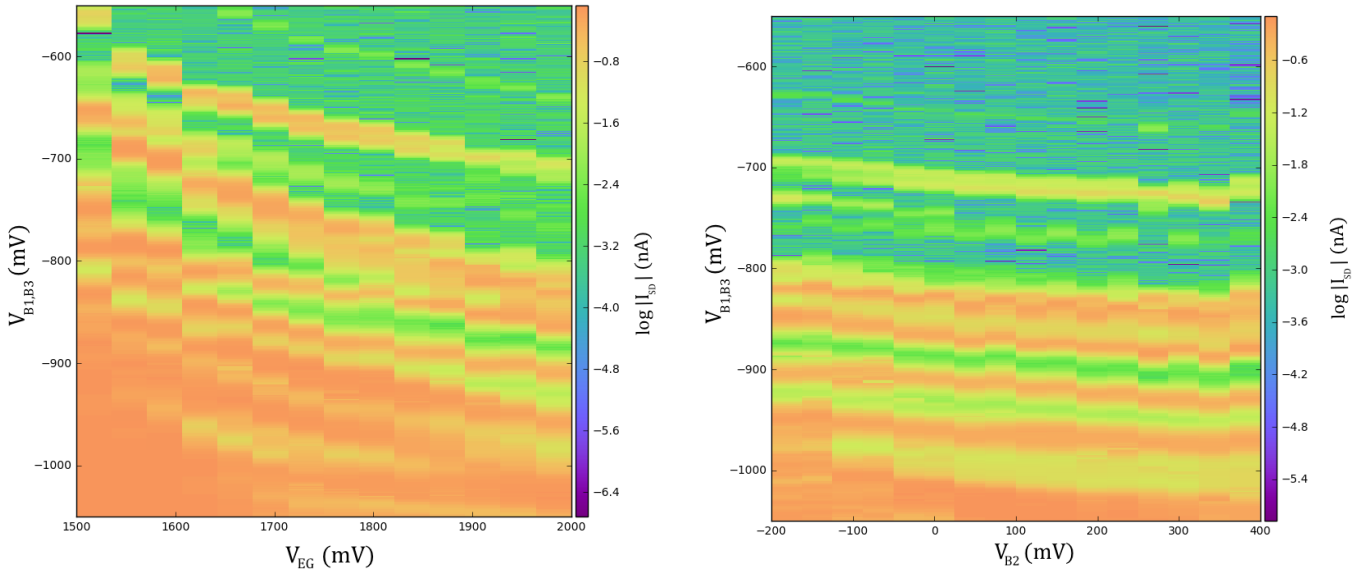


Figure 4.16: Source-drain current as a function of V_{B1} and V_{B3} , and the voltage applied to the gates at the electron operation region (left) or V_{B2} (right). Both measured again at $T \approx 4.2$ K for $V_{SD} = 1$ mV and $V_{L1} = V_{L2} = -2000$ mV. For the scan on the left $V_{B2} = 0$, while for the scan on the right $V_{EG} = 2000$ mV. The current is plotted in a logarithmic scale.

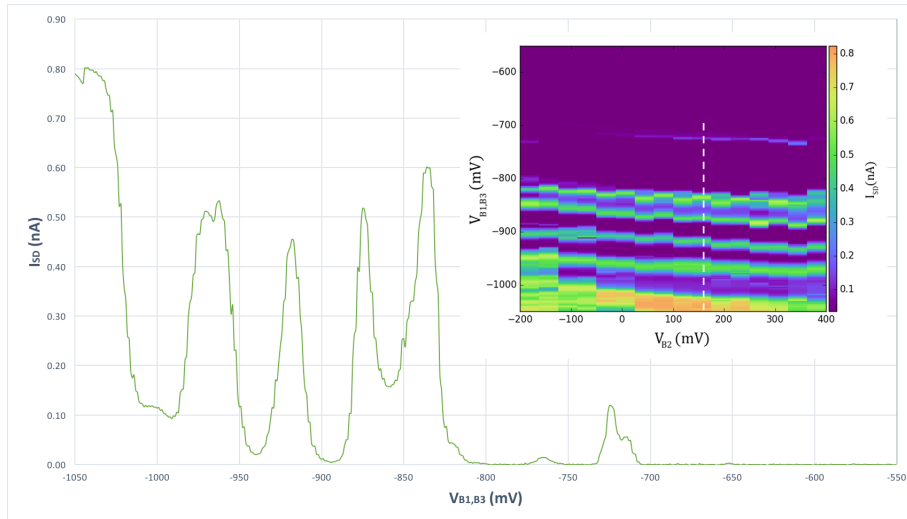


Figure 4.17: Coulomb peaks in the source-drain current measured at $T \approx 4.2$ K for $V_{B2} = 160$ mV, $V_{SD} = 1$ mV, $V_{L1} = V_{L2} = -2000$ mV, and $V_{EG} = 2000$ mV. Similar to the electron transport case discussed earlier, the Coulomb peaks show different heights and are irregularly spaced. Inset: the dashed line indicates the area of the barrier versus barrier scan where the Coulomb peaks were measured. Notice the linear current scale.

To conclude, the viability of the design of device II was showcased by the formation of an intentional quantum dot on the hole operation region at $T \approx 4.2$ K. The weak coupling to the second barrier, the incapability to influence the potential profile using the plunger gates, and the inability to form a double quantum dot due to the leakage between the first and third barrier, didn't allow us to further proceed with transport experiments.

5. CONCLUSION & OUTLOOK

In this project, we have successfully obtained quantum dots by electrostatic gating of a carrier gas in silicon. These dots were operated as single-charge transistors via multiple gates. In total, two different device architectures were tested. We have reported single-charge tunneling in a cryogenic environment for both electrons and holes.

For device I, we have demonstrated that it is possible to tune the electron transport at 4.2 K and 50 mK via its gates. Single and double intentional quantum dots were formed and its electron occupation was tuned down to the few-electron regime. Additionally, the ability of the device to operate as a charge sensor has been demonstrated. The hole operation region of this device was expected to show similar results, but we were unable to continue with hole-transport experiments since the device failed during testing.

A new device design was realized, that of device II, to obtain better control over the formation of the quantum dots and reach the single-charge regime in the dot occupancy. The capabilities of this design were demonstrated by the formation of an intentional quantum dot in the hole operation region. Alas, this particular device sample didn't function as expected, something that disallow us to further proceed with transport experiments. Multiple devices from the same sample chip were tested. Leakages between barriers were detected on various devices and a number of them didn't demonstrate a turn-on behavior. Nevertheless, in the past, experiments performed on similar device architectures achieved the formation of double quantum dots and demonstrated the ability to tune their electron occupation [35]. We therefore conclude that the design of device II has the potential to control single electrons and holes in silicon, but additional work is required during the device fabrication process to ensure their reliable operation during transport experiments.

There are numerous interesting phenomena that can be investigated in quantum dots after a reliable device has been fabricated. An example is using the Pauli spin blockade effect to detect and control the spin states of single spin carriers. This can be done, for example, by forming a double quantum dot and then tuning its potential such that successive electron transport requires a stage where two electrons must occupy the same dot. The electron transport then becomes spin-dependent [10]. Controlling the spins state of single carriers is a basic requirement for quantum information processing.

6. ACKNOWLEDGMENTS

Since this thesis started by referencing Richard Feynman, it would only have been appropriate to end with a quote of his: “We are lucky to live in an age in which we are still making discoveries”. Indeed, the research that takes place in the NanoElectronics group proves Feynman right. I am humbled to have been able to be part of this endeavor during my bachelor project.

I would like to thank all the people that made my bachelor thesis possible: my daily supervisor Sergey Amitonov for his patient guidance, valuable feedback on this report, help with the measurements during the last weeks of my project (event late at night on a Saturday) and for fabricating the samples I performed all the experiments on, Chris Spruijtenburg for helping me set up the measurement software and for helping me carry out the measurements when Sergey was busy, Floris Zwanenburg for providing me with the opportunity to work on this project and for being a member of my bachelor committee, Joost Ridderbos for giving me a first introduction to the world of quantum electronics, and Thijs Bolhuis for teaching me how to use the wire bonder. I would also like to thank Cora Salm for agreeing to serve as an external member of my bachelor committee. It was about three and a half years ago when during our first lecture in electrical engineering she introduced us to Ohm’s and Kirchhoff’s laws. Thankfully, this work has been more challenging than that.

Last but not least, I would like to thank Wilfred van der Wiel and the entire NanoElectronics group for making me feel welcomed during my bachelor assignment. NanoElectronics is, without a doubt, the coolest place in Twente.

APPENDIX A

Multiple Scanning electron microscope (SEM) images of device II are attached bellow. These images demonstrate issues during the fabrication process, such as gate damage, gate metal discontinuity, or even total absence of a gate electrode. For the design of this structure refer to figure 3.1 B.

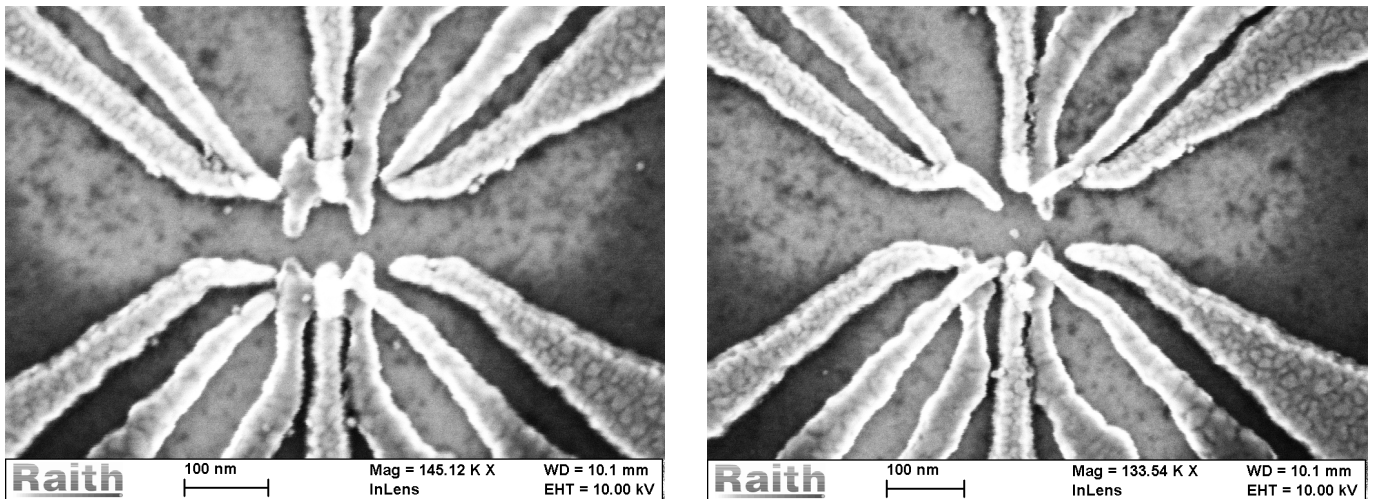


Figure A.1: Absence of part of (left) or the entire (right) barrier 1 electrode on the electron operation region.

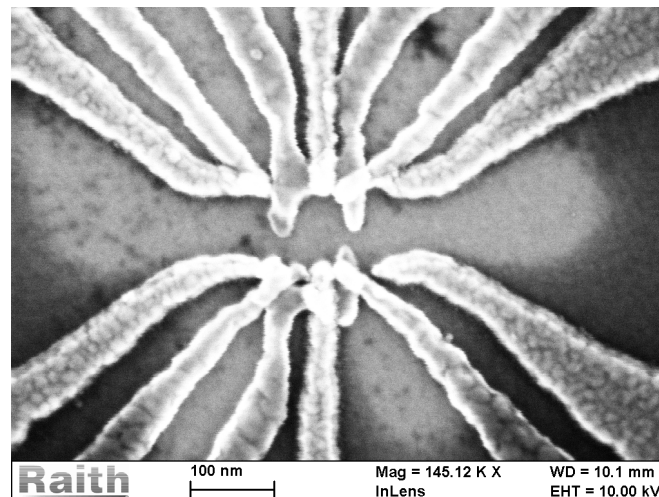


Figure A.2: Absence of part of barrier 3 electrode on the hole operation region.

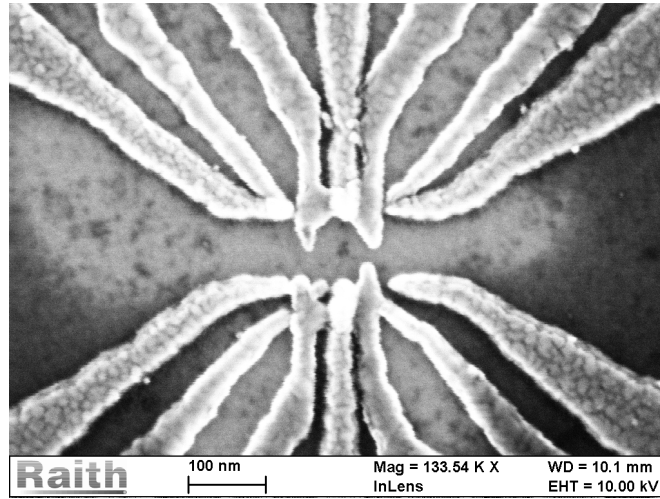


Figure A.3: Gate metal discontinuity and gate damage on multiple electrodes.

Additional measurements from the electron and hole operation region of device II.

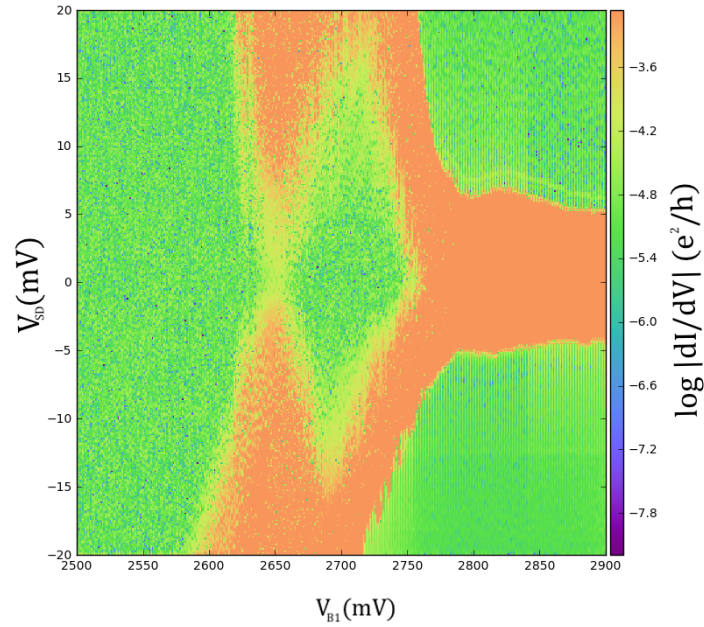


Figure B.1: Bias spectroscopy performed on the unintentional dot at the electron operation region of device II for $T \approx 4.2$ K and $V_{B2} = 600$ mV, $V_{L1} = V_{L2} = 3000$ mV, and $V_{HG} = -1000$ mV. A single, non-well resolved Coulomb diamond can be distinguished.

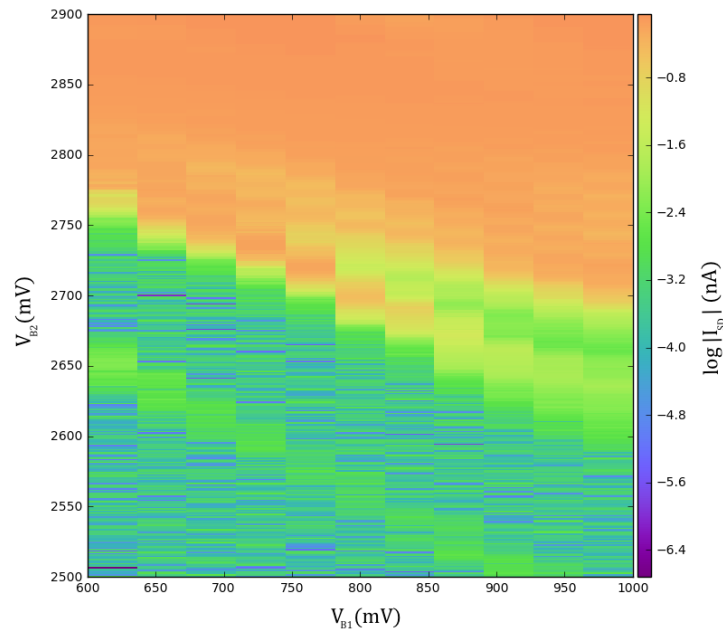


Figure B.2: Source-drain current of the electron operation region of device II as a function of V_{B1} and V_{B2} measured at $T \approx 4.2$ K for $V_{SD} = 1$ mV, $V_{L1} = V_{L2} = 3500$ mV, $V_{HG} = -1000$ mV and $V_{P1} = V_{P2} = 3000$ mV.

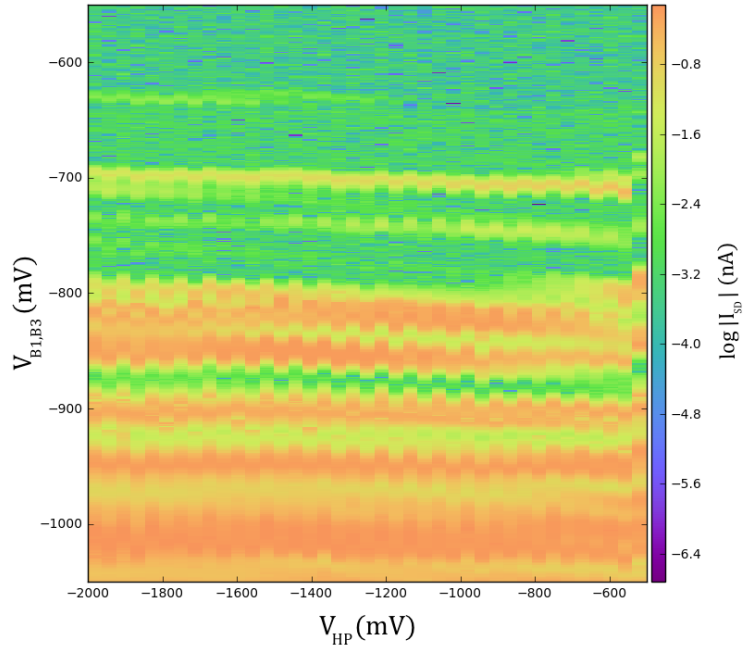


Figure B.3: Source-drain current of the hole operation region of device II as a function of V_{B1} and V_{B3} , and the voltage applied to the plunger gates of the electron operation region. Measured at $T \approx 4.2$ K for $V_{SD} = 1$ mV and $V_{L1} = V_{L2} = -2000$ mV, $V_{EG} = 2000$ mV and $V_{B2} = 0$. The parallel to x-axis transition lines indicate coupling only to the barrier gates.

BIBLIOGRAPHY

- [1] R.P. Feynman, Feynman Lectures on Computation, edited by A.J.G. Hey and R. W. Allen. Addison Wesley (1996).
- [2] B. E. Kane, “A silicon-based nuclear spin quantum computer”, Nature 393, 133 (1998).
- [3] P.W. Shor, “Algorithms for quantum computation: discrete logarithms and factoring”, in Proceedings of 35th Annual Symposium on Foundations of Computer Science, IEEE Press (1994).
- [4] W. van Dam et al., “Efficient Quantum Algorithms for Estimating Gauss Sums”, Arxiv.org (2002). Available: <http://arxiv.org/abs/quant-ph/0207131>. [Accessed: 08-Jan-2016].
- [5] A. Ambainis, “Quantum search algorithms”, Arxiv.org (2005). Available: <http://arxiv.org/abs/quant-ph/0504012>. [Accessed: 08-Jan- 2016].
- [6] G. Moore, “Progress in Digital Integrated Electronics”, in IEEE Electron Devices Meeting, IEEE Press (1975).
- [7] R. Hanson, Electron spins in semiconductor quantum dots. PhD thesis, Delft University of Technology (2005).
- [8] S.A. Wolf et al., “Spintronics: A Spin-Based Electronics Vision for the Future”, Science 294, 1488 (2001).
- [9] D.J. Griffiths, Introduction to Quantum Mechanics, Second Edition. Pearson Education (2005).
- [10] R. Hanson et al., “Spins in few-electron quantum dots”, Reviews of Modern Physics 79, 1217 (2007).
- [11] D. Loss and D.P. DiVincenzo, “Quantum computation with quantum dots”, Physical Review A 57, 120 (1998).
- [12] H. Christ, Quantum Computation with Nuclear Spins in Quantum Dots. PhD thesis, Technischen Universität München (2007).
- [13] G.W. Hanson, Fundamentals of Nanoelectronics. Pearson Education (2008).
- [14] L.P. Kouwenhoven et al., “Few-Electron Quantum Dots”, Reports On Progress in Physics 64, 701 (2001).

- [15] K.K. Likharev, "Single-Electron Devices and Their Applications", Proceedings of the IEEE (1999).
- [16] L.E. Brus, "Chemistry and Physics of Semiconductor Nanocrystals", columbia.edu (2007). <http://tinyurl.com/Semiconductor-Nanocrystals>. [Accessed: 08-Jan-2016].
- [17] L. Mangolini et al., "High-yield plasma synthesis of luminescent silicon nanocrystals", Nano Letters 5, 655 (2005).
- [18] D.L. Klein et al., "Fabrication of Metallic Electrodes with Nanometer Separation by Electromigration", Applied Physics Letters 68, 2574 (1996).
- [19] L. P. Kouwenhoven, C. M. Marcus, P. L. McEuen, S. Tarucha, R.M. Westervelt, and N.S. Wingreen, Mesoscopic Electron Transport. Plenum Publishing (1997).
- [20] S.W. Lee et al., "Ordering of quantum dots using genetically engineered viruses". Science 296, 892 (2002).
- [21] W.H. Lim et al., "Observation of the single-electron regime in a highly tunable silicon quantum dot", Applied Physics Letters 95, 242102 (2009).
- [22] C.H. Yang et al., 'Dynamically controlled charge sensing of a few-electron silicon quantum dot', AIP Advances 1, 042111 (2011).
- [23] G.J. Podd et al., "Charge Sensing in Intrinsic Silicon Quantum Dots", Applied Physics Letters 96, 082104 (2010).
- [24] F.A. Zwanenburg et al., "Silicon quantum electronics", Reviews of Modern Physics 85, 961 (2013).
- [25] A. Scholze, Simulation of single-electron devices. PhD thesis, Swiss Federal Institute of Technology Zurich (2000).
- [26] W.G. van der Wiel, Electron transport and coherence in semiconductor quantum dots and rings. PhD thesis, Delft University of Technology (2002).
- [27] A. Fuhrer, Phase Coherence, Orbital and Spin States in Quantum Rings. PhD thesis, Swiss Federal Institute of Technology Zurich (2003).
- [28] W.G. van der Wiel et al., "Electron transport through double quantum dots", Reviews of Modern Physics 75, 1 (2002).
- [29] J. Chuancheng et al., "Molecule-electrode interfaces in molecular electronic devices", Chemical Society Reviews 42, 5642 (2013).
- [30] S. J. Angus et al., "Gate-Defined Quantum Dots in Intrinsic Silicon", Nano Letters 7, 2051 (2007).

- [31] G. Dingemans et al., “Hydrogen induced passivation of Si interfaces by Al_2O_3 films and $\text{SiO}_2/\text{Al}_2\text{O}_3$ stacks”, Applied Physics Letters 97, 152106 (2010).
- [32] P. C Spruijtenburg et al., “Single-hole tunneling through a two-dimensional hole gas in intrinsic silicon”, Applied Physics Letters 102, 192105 (2013).
- [33] F. Müller, Single-Charge Tunneling in Ambipolar Silicon Quantum Dots. PhD thesis, University of Twente (2015).
- [34] S. Upadhyay, Few Electron Quantum Dots in InAs/InP Core Shell Nanowires. Master thesis, Delft University of Technology (2010).
- [35] N. S. Lai et al., “Pauli Spin Blockade in a Highly Tunable Silicon Double Quantum Dot”, Nature Scientific Reports 1, 110 (2011).